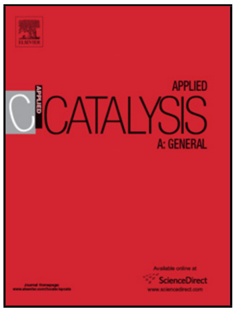

Highly active and poison-tolerant nickel catalysts for tar reforming synthesized through controlled hydrothermal synthesis

Dara Khairunnisa Binte Mohamed (Conceptualization) (Data curation) (Formal analysis) (Investigation) (Methodology) (Writing - original draft) (Writing - review and editing), Andrei Veksha (Conceptualization) (Data curation) (Formal analysis) (Methodology) (Supervision) (Writing - original draft) (Writing - review and editing), Teik-Thye Lim (Conceptualization) (Supervision) (Writing - review and editing), Grzegorz Lisak (Conceptualization) (Resources) (Supervision) (Writing - review and editing)

PII: S0926-860X(20)30372-0
DOI: https://doi.org/10.1016/j.apcata.2020.117779
Reference: APCATA 117779

To appear in: *Applied Catalysis A, General*

Received Date: 27 May 2020
Revised Date: 23 July 2020
Accepted Date: 12 August 2020

Please cite this article as: { doi: https://doi.org/

Highly active and poison-tolerant nickel catalysts for tar reforming synthesized through controlled hydrothermal synthesis

Dara Khairunnisa Binte Mohamed[a,b,c], Andrei Veksha[c,]*, Teik-Thye Lim[a,b,c], Grzegorz Lisak[a,b,c,]*

[a] School of Civil and Environmental Engineering, Nanyang Technological University, Singapore 639798, Singapore.

[b] Interdisciplinary Graduate School, Nanyang Technological University, Singapore 639798, Singapore.

[c] Residues and Resource Reclamation Centre, Nanyang Environment and Water Research Institute, Nanyang Technological University, 1 Cleantech Loop, CleanTech One, Singapore 637141, Singapore.

*Corresponding authors. Tel.: +65-6592-1756; fax: +65-6792-7319. *Email*: aveksha@ntu.edu.sg (A. Veksha) and g.lisak@ntu.edu.sg (G. Lisak).

Graphical abstract

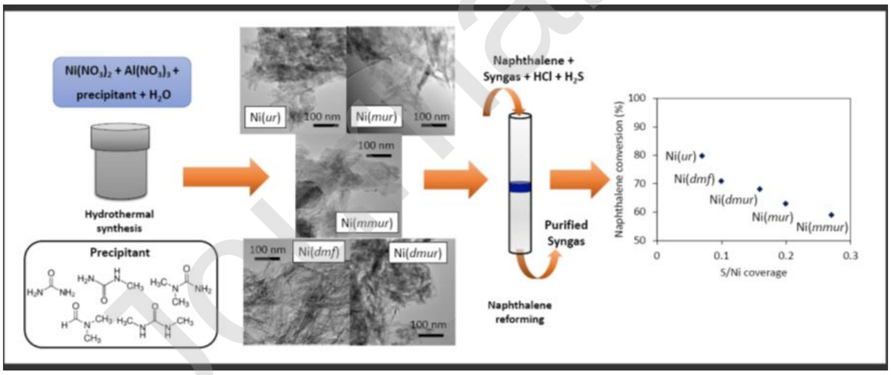

Highlights

- Hydrothermal synthesis of Ni catalysts using selected organic precipitants.
- Catalytic tar reforming in the presence of impurities for syngas purification.
- Catalysts exhibited high activity and resistance towards poisoning by impurities.

- Precipitants influenced distribution of Ni, improving tolerance to H_2S poisoning.
- Highly stable nickel aluminates contributed to high water-gas shift activities.

Abstract

Nickel catalysts suffer from the loss of tar reforming activity due to poisoning by syngas impurities. The strategy of increasing activity of catalysts through selection of suitable organic precipitants for hydrothermal synthesis was investigated. Catalysts were synthesized from nickel and aluminum nitrates using urea, N,N'-dimethylformamide, N-methylurea, 1,1-dimethylurea and N,N'-dimethylurea as precipitants and screened for naphthalene reforming. The catalyst prepared with urea maintained the highest reforming activity for 10 h in the presence of 50 ppmv H_2S (80% naphthalene conversion, 800 °C). This was attributed to lower chemisorption of sulfur on Ni sites, due to the larger percentage of Ni^0 and Ni aluminates which are less susceptible towards sulfidation than NiO. The precipitant also influenced the water gas shift activity which was higher in case of N,N'-dimethylformamide and urea probably due to Ni aluminate formation. Thus, a type of precipitant plays an essential role in tailoring of catalysts for syngas upgrading.

Keywords: catalytic reforming; hydrothermal synthesis; nanoflakes; nanospindles; naphthalene; nickel catalyst.

1. Introduction

Municipal solid waste (MSW) gasification is considered a viable alternative to waste incineration, as it produces syngas which can be further applied as a fuel for fuels cells and gas engines, or serve as a feedstock for chemical synthesis [1]. Raw syngas contains significant amounts of tar compounds, i.e., aromatic hydrocarbons formed from the thermal decomposition of complex organic compounds as well as other reactions related to the decomposition of feedstock [2]. The high content of tar in raw syngas poses an obstacle for syngas utilization. Tar compounds exist in the vapour form at gasification temperatures but condense upon cooling of the syngas causing clogging and corrosion of equipment. Tar removal is therefore an important aspect of syngas upgrading technology [3, 4].

A promising method of tar removal is catalytic tar reforming, which is carried out at temperatures close to the syngas temperature at the outlet of gasifier, and is advantageous as heat losses are minimized and liquid waste streams are not produced [5, 6]. Typically, nickel has been preferred as a reforming catalyst as it is highly active, low cost compared to noble metals, and commercially available [7]. Despite these advantages, Ni catalysts are susceptible to deactivation due to coke formation on the catalyst surface, Ni sintering as well as poisoning by syngas impurities [8]. It has been demonstrated that syngas impurities play essential role in the loss of catalytic activity of Ni based catalysts [9-15]. Studies by the Richardson group reported that chloride species from chlorocarbons had a detrimental effect on methane reforming and water-gas shift (WGS) reactions [10, 11]. HCl concentrations up to 2000 ppmv present in the gas during naphthalene steam reforming were shown to poison the WGS activity of Ni catalysts [12]. Sulfur species, such as H_2S and COS, presents a major problem for Ni reforming activity, and even a small amount of these species could poison Ni catalysts [13, 16-18]. The chemisorption of sulfur species by a Ni catalyst leads to a complexation between Ni and S, causing a reduction in available Ni active sites for hydrocarbon reforming [19]:

$$\mathrm{Ni_x} + x\mathrm{H_2S} \rightarrow \mathrm{NiS_x} + x\mathrm{H_2} \qquad (1)$$

The NiS complex has a high mobility over the catalyst surface due to the low melting point, which increases the sintering ability causing further deactivation of the Ni catalyst [20]. Additionally, studies have shown sulfur poisoning is likely to increase carbon deposition on a catalyst surface [16, 21-24]. According to Dou et al, when H_2S and HCl present together in syngas, a more pronounced poisoning of the WGS activity of the Ni catalyst was observed [9]. Considering that tar compounds co-exist with H_2S and HCl in syngas, development of tar reforming catalysts is essential to maintain high and durable activity in the presence of both impurities.

Several strategies have been explored to enhance the activity of tar reforming catalysts in the presence of syngas impurities. They include using acidic supports such as Al_2O_3 or basic supports such as CaO, doping of other metals to the Ni catalyst to form alloys, support modification as well as control of catalyst morphology [19, 25]. Previous studies on the development of sulfur tolerant catalysts have focused on using noble and rare earth metal dopants as promoters, such as La, Rh, Pd, and Ce [26-28]. Although the perovskite-based $LaNi_{0.5}Mn_{0.5}O_3$ catalyst was found to have higher tar reforming activity than a $LaNiO_3$ catalyst in the presence of 50 ppm H_2S, the catalyst without Ni, $LaMnO_3$, was even more resistant to the sulfur poisoning with much higher activities [26]. Bimetallic Rh-Ni/Ce-Al_2O_3 catalyst was shown to be more resistant to deactivation during a biogas tri-reforming process in the presence of 25 ppm H_2S, and was able to undergo regeneration and reverse the adverse effects of H_2S poisoning. [27]. High resistance to H_2S was also achieved by doping Ni catalysts with WO_3 which showed high activity at low reforming temperatures even in the presence of H_2S [29]. Although catalyst promoters have shown great promise in the development of poison-tolerant catalysts, synthesis using conventional metals such as Ni and alumina are preferred due to the low cost and their availability [30].

Catalysts on nanostructured supports also show superior catalytic activity than conventional catalysts, due to a better active Ni metal dispersion on the support [25]. Various preparation methods have been utilized in the synthesis of nanostructured catalysts [31]. One common synthesis method is a hydrothermal synthesis, in which the catalyst precursors are dissolved in a solvent followed by controlled precipitation under heat and pressure [32]. Reaction conditions, such as temperature and time, as well as the types and amounts of precursors were shown to influence the physical properties of the catalysts. [32]. A commonly used precipitant is urea, which slowly hydrolyses in water at elevated temperature and pressure allowing a more controlled increase of pH and precipitation of precursors [33, 34]. Other types of precipitants that have been used include sodium hydroxide [35], potassium hydroxide [36], hydrazine hydrate [37] and tetra-alkyl ammonium hydroxides [38], amongst others. Compared to urea which slowly increased the pH of the solution upon hydrolysis under heating, other precipitants were strongly basic leading to immediate precipitation of the catalyst precursors and severe agglomeration of particles, and as such, do not have a large impact on the control of the catalyst morphology. Ni-based catalysts used in hydrocarbon reforming that were synthesized using the urea-assisted hydrothermal method were found to have high surface areas and strong Ni-support interaction, which contributed to the high activities of the catalysts [39, 40]. Other than urea, the use of other amide-based organic precipitants with slow hydrolysis have not been extensively studied, and their effect on the catalyst activity and stability for tar reforming in the presence of syngas impurities are unknown.

Given the success of urea as a precipitant for the development of nanostructured catalysts, it is of great interest to explore the use of other types of amide-based organic precipitants with slow hydrolysis and investigate their effect on the physical and chemical properties of the catalyst, as well as on the catalyst activity. The objective of this study was to examine the effect of various precipitants on the catalytic activity and stability of the resulted nanostructured catalysts during tar reforming. Hydrothermal synthesis was employed to obtain the catalysts with controlled morphology and high Ni dispersion over alumina support. The catalysts were used in the reforming of naphthalene over a model syngas with H_2S and HCl, which are common syngas impurities. The effects of various precipitants on the nanostructure formation, Ni dispersion, Ni-support thermomechanical stability, resistance of catalysts to poisoning as well as Ni activity during tar reforming and water gas shift reactions are reported.

2. Experimental

2.1. Catalyst synthesis

Five catalysts were synthesized with different precipitants using the hydrothermal synthesis method. Catalysts were denoted as Ni (*x*), where *x* represents the precipitant, i.e. *ur* = urea (NH_2CONH_2, Sigma-Aldrich), *dmf* = N,N-dimethylformamide ($HCON(CH_3)_2$, Sigma-Aldrich), *mur* = N-methylurea ($CH_3NHCONH_2$, Sigma-Aldrich), *dmur* = 1,1-dimethylurea ($(CH_3)_2NCONH_2$, Sigma-Aldrich), and *mmur* = N,N'-dimethylurea ($(CH_3NH)_2CO$, Sigma-Aldrich). The catalysts were prepared by dissolving nickel(II) nitrate hexahydrate ($Ni(NO_3)_2{\cdot}6H_2O$, Sigma-Aldrich), aluminium nitrate nonahydrate ($Al(NO_3)_3{\cdot}9H_2O$, Sigma Aldrich) at a Ni/Al molar ratio of 0.12 and the required amount of catalyst precipitant in deionized water with a total solution volume of 120 mL. The total mole ratio of catalyst precursors ($Ni(NO_3)_2{\cdot}6H_2O$ and $Al(NO_3)_3{\cdot}9H_2O$) and precipitant, i.e. (Ni+Al) : precipitant, was 1:2 for *ur*, 1:3 for *mur, mmur* and *dmur*, and 1:15 for *dmf*. The mole ratios between (Ni+Al) : precipitant was chosen to ensure sufficient Ni and Al precipitation. The solution was transferred to a hydrothermal autoclave reactor with a 200 mL capacity and placed in an oven at 180 °C for 18 h. After the reaction and cooling, the formed precipitate was collected through filtration and washed for several times with water, dried in an oven at 100 °C overnight, and calcined for 5 h at 400 °C with a 10 °C min^{-1} ramping rate. After calcination, catalysts were crushed and sieved, and particles with sizes 100-315 μm were collected for testing.

A commercial catalyst with 6-hole monoliths (Xian Sunward Aeromat Co., China) was crushed and sieved, and 100 to 315 μm particle sizes were collected and used as a reference.

2.2. Catalyst characterization

Catalyst morphology was characterised with field emission scanning electron microscopy (JEOL JSM-7600F FESEM). Transmission electron microscopy (TEM) images of the catalysts were obtained using JEOL JEM-1400Plus Electron Microscope at 120 kV. Elemental mapping of the synthesized catalysts was conducted with Energy-Dispersive X-ray spectroscopy (EDX) analysis using an Oxford Instruments EDX detector coupled with TEM. High-resolution TEM was performed using TEM JEOL 2010 HR at 200 kV. Particle sizes of Ni particles in the spent catalysts were calculated from 150-200 Ni particles observed in TEM images using ImageJ software and assuming the Ni particles were spherical. ICP-OES was used to measure nickel content in catalysts (Perkin Elmer Optima 8300). BET surface areas, pore volumes and pore sizes of freshly prepared and spent catalysts were calculated from the N_2 adsorption and desorption isotherms measured at -196 °C with a Quantachrome Autosorb-1 Analyzer. Crystalline structure of the prepared and spent catalysts were obtained through X-Ray diffraction (XRD) analysis using a PANalytical XPert Pro XRD instrument with a radiation source of Cu-Kα. Samples were measured in a 10-80° 2θ range with a 0.035° step size and 0.3 s per step. X-ray photoelectron spectroscopy (XPS) analysis to determine Ni, S and Cl composition of spent catalysts was measured with a Kratos Axis Supra spectrophotometer with a dual anode monochromatic Kα excitation source. XPS peaks were processed using a CASA XPS software, and the binding energies for the elements analysed were calibrated using an adventitious carbon C 1s binding energy (284.8 eV). Temperature programmed reduction (TPR) was conducted by increasing the temperature to 900 °C at 10 °C min^{-1} in a gas mixture of 5% H_2/N_2 (30 mL min^{-1} flow rate). Elemental analyser for CHNS (Elementar Vario EL Cube) was used to measure carbon content in the fresh and spent catalysts.

2.3. Reforming of naphthalene

The prepared catalysts were applied for naphthalene reforming using a model syngas of H_2, steam, CO and CO_2 content that represented as close as possible real syngas composition, with the addition of H_2S and HCl to represent syngas impurities. The experimental setup for catalyst testing is shown in Fig. 1. Naphthalene, one of the major tar species and highly stable during reforming, was used as the representative tar compound [41]. An evaporator was used to vaporise naphthalene, which was then introduced into the system by flowing N_2 gas. Steam and HCl were introduced by feeding an aqueous solution of HCl with a syringe pump. Hydrogen gas was supplied during the experiments for catalyst reduction, as nickel is typically in the oxidized form in commercially available and lab-made reforming catalysts, and to provide a reducing environment throughout the reforming process. Steam and hydrogen concentrations introduced were 24 vol.% and 9 vol.%, which are within their reported ranges for the syngas produced from wet biomass and MSW [42, 43].

For each experimental run, a fixed-bed reactor with a frit (quartz, 50-90 μm openings) was loaded with 0.5 mL catalyst. The reactor was then heated to 800 °C (ramping rate = 15 °C min^{-1}) in a 20 vol. % H_2 – 80 vol. % N_2 gas mixture with a 50 mL-STP min^{-1} gas flow, and the catalyst was then reduced at 800 °C for 30 min. To perform the naphthalene reforming, a gas mixture with 0.055 vol. % naphthalene, 24 vol. % H_2O, 9 vol. % H_2, 10 vol%. CO, 9 vol. % CO_2, 0 or 50 ppmv H_2S, 300 or 2000 ppmv HCl and N_2 (balance) was flowed over the catalyst at 800 °C. The gas hourly space velocity was kept at 24000 h^{-1} with 200 mL-STP min^{-1} total gas flow rate. Naphthalene and gas samples were taken at hourly intervals for 10 h. Gas samples were collected into Tedlar bags for 5 min and analysed using a calibrated gas chromatograph (Agilent 7890B, USA) with two thermal conductivity detectors and a flame ionization detector. Naphthalene samples (in approximately 200 mL of gas flow) were collected using an air pump (Gilian GilAir Plus) and measured by solid phase adsorption (SPA) using Bond Elut NH_2 (500 mg, 3 mL, Agilent). Naphthalene was eluted from SPA tubes into a vial with 2 mL of dichloromethane and further diluted with a ratio of eluate to dichloromethane of 1:10. The solution was analysed with a calibrated gas chromatograph-mass spectrometer (Agilent 7890B GC and a 5977A MSD). Naphthalene samples at the outlet of the reactor were collected before and after the reforming experiments. Naphthalene conversion was calculated by using the following equation:

$$\text{Naphthalene conversion (\%)} = \frac{C_{\text{naphthalene, in}} - C_{\text{naphthalene, out}}}{C_{\text{naphthalene, in}}} \times 100\% \qquad (2)$$

where C is the concentration of naphthalene derived from the GC-MS analysis in g Nm^{-3}.

The results of all experiments are presented as averages of triplicated runs and standard deviations (±). Statistical significance was determined using an ANOVA method with a 95% confidence interval.

3. Results and discussion

3.1. Properties of catalysts

Chemical structures of the precipitants used in this study are shown in Fig. 2. During hydrothermal synthesis, the organic precipitants selected for the synthesis of catalysts undergo slow hydrolysis generating various reaction products. Specifically, the hydrolysis of urea generates ammonia and carbon dioxide (equation 3) [33]. The hydrolysis of other methylated urea derivatives generates carbon dioxide as well as methylamine and dimethylamine, depending on the amine functional group (equations 4-6). In contrast, the hydrolysis of N,N'-dimethylformamide produces dimethylamine and formic acid (equation 7). Hydrolysis of all precipitants increases the pH of solution causing the precipitation of catalyst precursors.

Urea (*ur*): $CO(NH_2)_2 + H_2O \rightarrow 2\,NH_3 + CO_2$ (3)

N-methylurea (*mur*): $CH_3NHCONH_2 + H_2O \rightarrow NH_3 + NH_2CH_3 + CO_2$ (4)

N,N'-dimethylurea (*mmur*): $CH_3NHCONHCH_3 + H_2O \rightarrow 2\,NH_2CH_3 + CO_2$ (5)

1,1-dimethylurea (*dmur*): $(CH_3)_2NHCONH_2 + H_2O \rightarrow NH_3 + (CH_3)_2NH_2 + CO_2$ (6)

N,N'-dimethylformamide (*dmf*): $(CH_3)_2NHCOH + H_2O \rightarrow (CH_3)_2NH_2 + HCOOH$ (7)

The formation of different reaction products during hydrothermal synthesis had a drastic effect on the shape and nanostructure of resulting catalysts. Fig. 3 shows the FESEM, TEM and HRTEM images of prepared catalysts. Fig. 3a demonstrates the morphology of Ni(*ur*) prepared with urea as a precipitant. According to FESEM and TEM images, the usage of urea resulted in the formation of flat, mostly rectangular nanoflake structures with varying dimensions, ranging from 50 to 150 nm in length and 10 to 35 nm in width. Using methylated urea derivatives, i.e. N-methylurea and N,N'-dimethylurea (Fig. 3b and Fig. 3c, respectively), catalysts with similar morphology to Ni(*ur*) were produced. The nanoflake sizes of Ni(*mur*) were between 35-160 nm (length) and 12-30 nm (width), which are close to the sizes of Ni(*ur*). However, the sizes of Ni(*mmur*) nanoflakes were larger, ranging from 75 to 200 nm and 30 to 115 nm in length and width, respectively. The HRTEM images show the lattice spacing of the catalysts. The lattice spacings for Ni(*ur*), Ni(*mur*) and Ni(*mmur*) were 0.44 nm, 0.46 nm and 0.46 nm respectively, corresponding to the (111) plane of Al_2O_3, which suggests the preferential growth of crystallites along the (111) plane for these catalysts. The differences in the lattice spacing values is due to the low crystallinity of the support which prevents an accurate measurement of the spacings, of which the (111) plane corresponds to a lattice spacing of 0.45 nm [44]. In contrast, the FESEM and TEM images of Ni(*dmf*) catalyst (Fig. 3d) show the presence of nanospindles with the length of 11-45 nm. According to the HRTEM image, the nanospindle shape was formed through the onion-like layering of alumina support containing well dispersed nickel species. Ni(*dmur*) (Fig. 3e) consisted of a mixture of nanoflakes and nanospindles, resembling the two nanostructures found in Ni(*ur*) and Ni(*dmf*), respectively. The nanoflake particle sizes of Ni(*dmur*) were in the range of 16-46 nm for length and 2-18 nm for width. From the HRTEM images of Ni(*dmur*) and Ni(*dmf*), the lattice spacings were 0.46 nm and 0.45 nm respectively, corresponding to (111) plane, however, the difference in the lattice spacing values indicates inaccurate measurement due to the low crystallinity of the support. According to these images, the formation of nanoflakes was favored by the precipitants that produce ammonia and methylamine during hydrolysis (i.e. urea, N-methylurea and N,N'-methylurea), while the formation of nanospindles was favored by N,N'-dimethylformamide which hydrolyzes to dimethylamine. Since 1,1-dimethylurea (*dmur*) decomposes into both ammonia and dimethylamine upon hydrolysis, Ni(*dmur*) contained both nanoflake and nanospindle structures. The differences in the morphologies of the synthesized catalysts were due to the hydrolysis products of the precipitants formed during the hydrothermal synthesis. The mixture of different compounds in the reaction solution (e.g. NH_3 and CO_2 from the hydrolysis of urea, CH_3NH_2 and CO_2 from the hydrolysis of N,N'-dimethylurea) affected the precipitation of Ni and Al precursors differently according to the different precipitant used [45]. The obtained morphology of catalysts was different from those reported previously [46, 47]. Controlled hydrothermal synthesis using hydrazine monohydrate was reported to yield square-shaped nanoflake γ-Al_2O_3 [46]. The hydrothermal synthesis of Ni-Al mixed oxide that was derived from a Ni-Al double layer hydroxide using urea as a precipitant resulted in flat circular nanosheets [47]. The differences in morphology obtained in this study could be due to the different synthesis conditions.

Using the hydrothermal synthesis method allowed to obtain well dispersed Ni species over the support as suggested by Fig. 4. According to the TEM-EDX images, Ni was uniformly distributed in the Al oxide matrix of all catalysts. The isotherms of N_2 adsorption-desorption is shown in Fig. 5a suggesting that the synthesized catalysts were mesoporous. The N_2 uptake occurred mainly at $P/P_o >$

0.1, with hysteresis loops between the adsorption and desorption branches of the isotherms. The properties of developed catalysts are shown in Table 1. The Ni content in the catalysts was 9-10 wt.%, whereas the commercial catalyst contained 16 wt.% Ni. Commercial catalyst had the highest Ni load per bed volume, due to the higher Ni content and larger bulk density. Among the synthesized catalysts, the Ni load per bed was the highest for Ni(*ur*), i.e. 0.03 g per 0.5 mL of catalyst, due to the largest bulk density (i.e. 0.62 g mL^{-1}). BET surface areas and total pore volumes of the developed catalysts were much larger than those of commercial catalyst (i.e. 183-243 m^2 g^{-1} and 0.24-0.70 mL g^{-1} for synthesized catalysts, respectively, compared to 20 m^2 g^{-1} and 0.01 mL g^{-1} of the commercial catalyst). Catalysts containing nanospindle structures had larger BET surface areas and total pore volumes than catalysts containing nanoflake structures. These results suggest that the selected type of precipitant can significantly influence the morphology and porosity of the catalyst during synthesis. Porosity plays an important role in hosting Ni nanoparticles and increasing surface active sites due to the deposition of Ni nanoparticles inside the porous cavities of the alumina support as well as providing the reacting species access to the active sites, thus influencing the catalytic activity [48].

Fig. 5b shows the XRD patterns of the prepared catalysts. The XRD patterns had broad peaks of both NiO and Al_2O_3 which indicated the formation of nanocrystallites of NiO, while Al_2O_3 in the catalysts had nanosized and/or non-crystalline structures. Ni aluminate peaks were not easily observed in the XRD pattern for all catalysts, due to the overlapping of peaks with those of γ-Al_2O_3, as well as the non-crystallinity and/ or high dispersion of Ni aluminates in the catalyst. Conversely, the XRD spectrum of commercial catalyst consisted of sharp peaks of both NiO and Al_2O_3, suggesting higher crystallinity of the Ni and Al compounds and lower dispersion of Ni. According to the XRD patterns, alumina support in the synthesized catalysts was in the form of γ-Al_2O_3, while in commercial catalyst it was in the form of α-Al_2O_3 [44]. γ-Al_2O_3 has a highly amorphous and porous structure, which would explain the highly porous nature of the synthesized catalysts and higher Ni dispersion [49]. Sharper NiO peaks could be observed in Ni(*ur*) indicating higher crystallinity of NiO compared to the other synthesized catalysts.

The TPR profiles of the developed catalysts are shown in Fig. 5c. From the TPR data the reducibility of NiO can be deduced and the strength of the interaction between Ni species and the Al_2O_3 surface can be confirmed. The TPR profiles of all catalysts contained varying reduction peaks, which suggests that Ni dispersion and interaction with the support varied among the catalysts [50, 51]. Ni(*ur*) and Ni(*mur*) had low temperature reduction peaks at 410 °C and 330 °C respectively, which correspond to the reduction of NiO weakly bound to the support [51]. Reduction peaks between 500-760 °C in the moderate temperature range correspond to NiO strongly bound to Al_2O_3 [50, 51]. Ni(*mur*), Ni(*dmf*) and Ni(*dmur*) had small reduction peak at 530 °C, while Ni(*ur*) had a reduction peak at 580 °C. Ni(*dmur*) also had a peak at 690 °C, while Ni(*mmur*) had a maximum intensity peak at 730 °C. The reduction peaks above 800 °C were also observed. The reduction peaks of Ni(*mur*) and Ni(*dmur*) were at 845 °C, while the peaks of Ni(*ur*) and Ni(*dmf*) were at 920 °C and 945 °C respectively, which could be attributed to nickel aluminates reduction [52-54].

The synthesized catalysts were characterized by Ni 2p XPS (Fig. 6). Apart from the binding energy (BE) of ~862 eV due to the shake-up satellite peak, the deconvolution of main Ni peak showed the presence of two Ni^{2+} states with BE of 855.6-855.7 and 856.6-856.7 eV, depending on the catalyst. The BE of unsupported Ni^{2+} in Ni-based catalysts is ~854 eV and increases with the strength of NiO–Al_2O_3 interactions to ~ 856 eV for NiO strongly bound to Al_2O_3 [55]. The Ni^{2+} peak at ~ 856-857 eV can be ascribed to nickel aluminate [53, 56]. According to the XPS spectra, all the synthesized catalysts contained strongly bound NiO and nickel aluminate on the surface. Table 2 provides the distribution of Ni^{2+} species calculated from the corresponding peak areas. Among the catalysts, Ni(*dmur*) contained higher amounts of nickel aluminate, suggesting NiO and alumina on the catalyst surface underwent higher solid state reaction. The Al 2p and O 1s spectra for the synthesized catalysts (Fig. S1) show peaks at ~74 eV and ~531 eV respectively, which indicated the presence of aluminium and nickel oxides, as well as that of Ni aluminates [57-59]. The TPR data (Fig. 5c) for Ni(*ur*) suggested the presence of weakly interacting NiO-Al_2O_3, which is not observed in surface of the catalyst by XPS analysis. This could be due to the low XPS sampling depth, which is less than 10 nm

[60, 61] and unable to detect Ni beneath the top surface layer. It can be seen from the characterization data that the properties of synthesized catalysts varied significantly with the type of precipitant. This could be attributed to the differences in decomposition pathways of precipitants and reaction products. In this respect, tailoring of catalyst properties using appropriate precipitants can provide a valuable approach towards designing catalysts with high catalytic activity.

3.2. Effect of precipitants on naphthalene reforming

To investigate the influence of precipitants on catalytic activity, the catalysts were employed in the reforming of naphthalene with the presence of syngas impurities such as H_2S and HCl. Fig. 7a shows the effect of impurities on the reforming efficiency of naphthalene over Ni(*ur*). Three conditions were tested: 2000 ppmv HCl + 50 ppmv H_2S, 300 ppmv HCl + 50 ppmv H_2S and 2000 ppmv HCl + 0 ppmv H_2S. From the analysis of the sampled gas, the products of the reforming for all catalysts were H_2, CO_2 and CO whereas C_1-C_5 hydrocarbons were not detected. It can be seen that at 0 ppmv H_2S and 2000 ppmv HCl, nearly complete conversion of naphthalene was maintained for 10 h. According to the thermodynamic calculations that were performed using an HSC Chemistry 9 software, the equilibrium naphthalene conversion was expected to be 100% in the presence of HCl, which is consistent with the experimental results. When both 50 ppmv H_2S and 2000 ppmv HCl were present, the activity decreased to 80±7% due to poisoning. There was no statistically significant increase in the reforming activity when HCl concentration was decreased from 2000 to 300 ppmv in the presence of H_2S (88±3% naphthalene conversion), suggesting that the loss of catalytic activity was primarily due to the presence of H_2S, whereas HCl had little effect on the reforming activity. Considering the observed impact of low concentration of H_2S on reforming activity, H_2S is a more potent catalyst poison compared to HCl. These results are consistent with the observations made during naphthalene steam reforming over various commercial and synthetic Ni-based catalysts under experimental conditions of 10 vol.% H_2, 26 vol.% H_2O and 14 vol.% N_2 [9, 12]. The newly obtained data suggested that the effects of HCl and H_2S on catalytic activity persist with the addition of CO and CO_2 to the gas stream. The detrimental effect of H_2S on reforming activity is typically attributed to the reaction of Ni and S leading to 1) the formation of inactive Ni-S complex, and 2) increased Ni sintering/decreased surface area due to higher Ni mobility caused by lower melting point of Ni-S species .

Fig. 7b shows the naphthalene reforming activity of catalysts synthesized using various precipitants in the presence of 50 ppmv H_2S and 2000 ppmv HCl. Although the Ni content in Ni(*ur*) used in the catalyst bed was 4 times lower than that in the commercial catalyst, the reforming activity of Ni(*ur*) was better than that of the latter, while Ni(*dmf*) and Ni(*dmur*) activities were comparable to the commercial catalyst even with lower Ni contents, suggesting superior activity. This could be attributed to higher Ni dispersion in the prepared catalysts, which is essential for the high reforming activity. The reforming activity of all tested catalysts decreased during 10 h tests due to poisoning. However, the loss of catalytic activity varied depending on the catalyst as suggested by the conversion efficiencies calculated within the last two hours of testing. While the reforming activity of Ni(*ur*), Ni(*dmf*), Ni(*mur*) and Ni(*mmur*) continued to decrease throughout the 10 h tests, the naphthalene conversion of Ni(*dmur*) stabilized to ~67% after 2 h until the end of the experiment. This could be attributed to the high pore volume of Ni(*dmur*) which maintained access for reacting species to be exposed to the active Ni. Ni(*ur*) catalyst had the highest reforming activity (naphthalene conversion of 80%) followed by Ni(*dmf*) (naphthalene conversion of 71%) and the three other synthesized catalysts. There were no statistically significant differences between the catalytic activities of Ni(*dmur*), Ni(*mur*) and Ni(*mmur*). These reforming data cannot be attributed to the differences in Ni contents per bed volume shown in Table 1. Among the synthesized catalysts, the content of Ni was the lowest in Ni(*dmf*) while the activity of catalyst was one of the highest. To investigate whether the morphology and porosity influenced the reforming activity, the BET surface areas and pore volume data of the spent catalysts was measured and the results are shown in Table S1. After reforming, the surface areas of the catalysts decreased, After reforming, the surface areas and pore volumes of the catalysts decreased, with Ni(*ur*) having a surface area of 110 $m^2 g^{-1}$ and total pore volume of 0.269 mL g^{-1}, while surface areas of Ni(*dmf*) and Ni(*dmur*) decreased more drastically (115 and 116 $m^2 g^{-1}$

respectively), the total pore volumes remained high (0.394 and 0.461 mL g^{-1} respectively). While porosity plays an important role in the reforming activity of the catalyst [62], it was found that high reforming activities could also be achieved with catalysts having lower surface area and porosity, as suggested by Veksha et al [12]. In this case, the differences in reforming activity of the catalysts were not solely due to the different surface areas and pore volumes. Rather, the use of different precipitants influenced Ni dispersion, as shown in the TPR results (Fig. 5c), with varied reduction peaks of NiO indicating strong Ni-support interaction and thus higher activities.

Coke formation is known to influence catalyst deactivation [63]. To determine whether carbon deposition occurred on the Ni particles during reforming, TEM images of the spent catalysts were obtained and shown in Fig. 8. In the TEM images, Ni species are represented by the distinct dark spherical particles scattered across the support matrix. From observation of the Ni particles in the TEM images of the catalysts, filamentous or encapsulating carbon that can deactivate the catalyst were not formed [63-65]. CHNS analysis was performed to determine the carbon, hydrogen, nitrogen and sulfur content in the fresh and spent catalysts. From the analysis, an increase in the carbon concentration of the spent catalysts compared to the fresh catalyst could indicate carbon deposition on the catalysts. The carbon contents in the fresh and spent catalysts were below detection limits, confirming that carbon deposition on the catalysts did not occur. This could be due to the high steam content in gas (24 vol%) taking part in carbon gasification.

In order to investigate the role of syngas impurities on the loss of activity, the spent catalysts were characterized using XPS. The wide survey XPS spectra suggested the presence of both Cl and S species chemisorbed on the spent catalysts (Fig. S2). As it was discussed above, there was HCl did not affect the reforming activity significantly and the poisoning effect could be primarily attributed to S chemisorption on Ni surfaces [66, 67]. Fig. 9 shows the relationship between the naphthalene conversion of catalysts and S/Ni ratios calculated from the XPS survey spectra. The S/Ni ratios correspond to the surface coverage of Ni atoms with chemisorbed S species. Naphthalene conversion was found to decrease with increasing S/Ni ratio, suggesting that the higher S chemisorption could reduce the tar reforming activity of catalysts.

Using an HSC Chemistry 9 software, thermodynamic calculations were carried out to investigate the reasons for different extents of Ni coverage by S among the synthesized catalysts. It was assumed that Ni can be present in three states on the catalyst surface, namely Ni, NiO and $NiAl_2O_4$. During reforming, metallic Ni is formed due to reduction by H_2, while Ni^{2+} compounds can exist on the catalyst surface due to the oxidation by H_2O, which is more favourable in the presence of alumina support facilitating NiO-support interactions [9]. The possible reactions between the Ni compounds and H_2S are as follows:

$$Ni + H_2S \rightarrow NiS + H_2 \qquad \Delta G° = -30.3\ kJ\ mol^{-1} \quad (8)$$

$$NiO + H_2S \rightarrow NiS + H_2O \qquad \Delta G° = -76.7\ kJ\ mol^{-1} \quad (9)$$

$$NiAl_2O_4 + H_2S \rightarrow NiS + \gamma\text{-}Al_2O_3 + H_2O \qquad \Delta G° = -46.0\ kJ\ mol^{-1} \quad (10)$$

It can be seen from the negative standard Gibbs energies (ΔG°) at 800 °C that all three reactions can occur spontaneously at the reforming temperature. However, the reaction between NiO and H_2S (equation 9) is the most thermodynamically favourable due to the lowest ΔG° followed by $NiAl_2O_4$ and Ni (equations 10 and 8, respectively). These results suggest that, during the reforming, sulfidation of oxidized Ni compounds is more favorable compared to metallic Ni. Furthermore, the differences in the ΔG° values for NiO and $NiAl_2O_4$ imply that the Ni poisoning by H_2S could be influenced by the strength of NiO-Al_2O_3 interactions (i.e. the sulfidation of NiO weakly bound to the support is more favorable). Previously, Blanchard et al. found that the loss of the $NiAl_2O_4$ phase of an $NiAl_2O_4/Al_2O_3$-YSZ catalyst during methane dry reforming resulted in higher deactivation rates from H_2S poisoning, and that reforming the spinel $NiAl_2O_4$ phase could successfully regenerate the catalyst [68]. This shows that H_2S poisoning could be more detrimental to catalyst activity depending on the different forms of Ni in the catalyst.

The XPS characterization of the spent catalysts was carried out to identify Ni species present on the surface of the catalyst. The distribution of Ni species determined by deconvolution of the core

Ni 2p peaks is shown in Fig. 10. All catalysts contained the peaks at (1) 852.7-852.8 eV indicative of Ni^0 (Peak 1) (2) 855.7-855.9 eV indicative of strongly bound NiO (Peak 2), and (3) 856.7-856.9 eV indicative of nickel aluminate (Peak 3). The quantification of identified species in accordance with Peak 1, 2 and 3 intensities are shown in Table 3. Based on the thermodynamic data, catalysts with high amounts of surface Ni^0 (Peak 1) and nickel aluminates (Peak 3) are less likely to react with H_2S. The total contents of Ni^0 and nickel aluminates were the highest in Ni(*ur*) (65.5%), followed by Ni(*dmf*) (63.3%), Ni(*dmur*) (59.2%), Ni(*mur*) (57.8%) and Ni(*mmur*) (56.9%), which explains the decrease in S chemisorption on catalysts in the same order. These data suggest that the tolerance to sulfur poisoning and high catalytic stability of catalysts during reforming could be greatly influenced by the state of Ni species. The contents of Ni^0, NiO and nickel aluminates are determined by the type of precipitant used for the catalyst synthesis.

Table 4 compares the reforming activity of the selected synthesized catalyst, i.e. Ni(*ur*), with catalysts that were tested in the presence of H_2S in other studies. Besides the higher activity compared to the commercial catalyst, which was included into this work, Ni(*ur*) showed higher activity compared to the reported Ni, Ni-Fe and Ni-Ce catalysts supported on Al_2O_3 [9, 17, 69, 70], Rh-Ni catalyst supported on Ce-Al_2O_3 [27] and $LaNi_{0.5}Mn_{0.5}O_3$ [26]. This demonstrates the high potential of the proposed synthesis method towards the fabrication of poison-tolerant catalysts for tar reforming.

3.3 Effect of precipitants on water-gas shift

Under steam reforming conditions, water-gas shift (WGS) reaction (equation 11) from the reaction of excess steam with CO to form CO_2 will occur. Similarly, the addition of steam to a dry reforming process will allow this reaction to take place.

$$CO + H_2O \leftrightarrow CO_2 + H_2 \qquad (11)$$

In order to examine the extent of WGS reaction during the reforming of naphthalene with 2000 ppmv HCl and 50 ppmv H_2S, the CO/CO_2 ratios were calculated for the outlet gas and are shown in Fig. 11. A low CO/CO_2 ratio indicates higher WGS reaction as CO is consumed and CO_2 produced.

The dashed line corresponds to the CO/CO_2 ratio at thermodynamic equilibrium. The CO/CO_2 ratios of all catalysts were close to the equilibrium value at the start of the reaction and subsequently increased rapidly within 1 h before stabilization. The increase in CO/CO_2 ratios was less prominent between 1 and 10 h of testing. Higher CO/CO_2 ratios suggest the loss of WGS activity by catalysts. The WGS activities of the synthesized catalysts were higher than the commercial catalyst. Ni(*dmf*) had the highest WGS activity followed by Ni(*ur*), Ni(*dmur*), Ni(*mur*) and, finally, Ni(*mmur*). This trend was different compared to that for the reforming activities, suggesting that the type of precipitant had different influence on the WGS activities.

One reason for the deactivation of WGS activity could be the sintering of Ni particles as a result of chemisorption by HCl [12]. The Ni sintering is irreversible and occurs due to either Ni migration and coalescence or Ostwald ripening [71, 72]. The XRD spectra of spent catalysts (Fig. S3) showed the appearance of sharp peaks of metallic Ni indicating that Ni crystallite sizes increased during reforming confirming the sintering, while more intense γ-Al_2O_3 peaks were observed, due to the increased crystallinity from the annealing of the support particles. The Ni particle size distributions of the synthesized and commercial catalysts after 10 h of reforming with 2000 ppmv HCl and 50 ppmv H_2S calculated from the TEM images of 150-200 particles are shown in Fig. 12. According to the smaller sizes of Ni particles, the synthesized catalysts were more resistant to sintering compared to the commercial catalyst. In the synthesized catalysts, Ni particles had sizes between 10 and 100 nm, while in the commercial catalyst, Ni particles with sizes only above 50 nm were observed. The smaller sizes of Ni particles could explain higher WGS activities of the synthesized catalysts compared to the commercial catalyst. These data reflect the excellent capability of the synthesized catalysts towards sintering resistance in the presence of syngas impurities. The sintering resistance is attributed to the strong interactions between Ni^{2+} and the alumina support preventing agglomeration of Ni during reforming [73, 74]. XPS data suggest that all the spent catalysts contained Ni^{2+} species with high binding energies, attributed to either strong NiO-support interactions or $NiAl_2O_4$ formation (Peaks 2 and 3 in Table 3, respectively). It was suggested previously that while reforming activity to the larger extent depends on the presence of Ni^0 species, the WGS activity is facilitated by the presence of Ni^{2+} species formed at the Ni-alumina interface. Hence, the strength of the Ni-support interaction is important in providing stable oxygenated Ni^{2+} for WGS reaction [75, 76]. The interactions are higher in the case of smaller Ni particles due to the larger contact area with the support.

The TPR profiles (Fig. 5c) of the catalysts show that both Ni(*ur*) and Ni(*dmf*) had reduction peaks higher than the reforming temperature of 800 °C, suggesting highly stable nickel aluminates were present. According to the reduction peaks, the stability of nickel aluminates was higher in Ni(*dmf*) compared to Ni(*ur*) (reduction temperatures 945 and 920 °C, respectively). This could be a reason for the higher WGS shift activity of the catalyst. The obtained data demonstrate the significant role that a precipitant play in the synthesis of catalysts with high reforming and WGS activities in the presence of poisons.

4. Conclusions

This study demonstrated that highly active and durable Ni-alumina catalysts can be synthesized from hydrothermal synthesis using selected organic precipitants. The precipitants used for catalyst synthesis were urea, N,N'-dimethylformamide, N-methylurea, 1,1-dimethylurea and N,N'-dimethylurea. The catalysts were employed in the reforming of naphthalene in the presence of HCl and H_2S as syngas impurities. The hydrolysis products of the precipitants influenced the morphology, Ni dispersion, porosity, Ni-alumina interaction and distribution of different Ni^0, NiO and $NiAl_2O_4$ species. It was found that the catalyst prepared using urea as a precipitant, Ni(*ur*), had the highest reforming activity. with 80% naphthalene conversion, followed by the catalyst prepared using N,N'-dimethylformamide, Ni(*dmf*), with 71% conversion of and the catalysts prepared using the remaining precipitants. The higher reforming activity was due to the lower chemisorption of S species on Ni and increased resistance towards H_2S poisoning. XPS data and thermodynamic calculations suggested that this was caused by the larger percentage of Ni^0 and Ni aluminates which are less susceptible towards sulfidation than NiO. Both N,N'-dimethylformamide and urea also influenced the high WGS activities for Ni(*dmf*) and Ni(*ur*). This is attributed to the high amount of Ni aluminates that were stable at high temperatures, which served as active sites for WGS reactions to take place. The choice of precipitant used during synthesis plays an important role in producing catalysts that can maintain high reforming and WGS activities, thus opening new insights for synthesizing catalysts that are highly active, stable, and tolerant towards poisoning for syngas upgrading.

Author contributions

Dara Khairunnisa Binte Mohamed: Conceptualization; Data curation; Formal analysis; Investigation; Methodology; Writing - original draft; Writing - review & editing.
Andrei Veksha: Conceptualization; Data curation; Formal analysis; Methodology; Supervision; Writing - original draft; Writing - review & editing.
Teik-Thye Lim: Conceptualization; Supervision; Writing - review & editing.
Grzegorz Lisak: Conceptualization; Resources; Supervision; Writing - review & editing.

Declaration of interests

The authors declare that they have no known competing financial interests or personal relationships that could have appeared to influence the work reported in this paper.

Acknowledgements

The authors would like to thank the Interdisciplinary Graduate Programme (IGP) and Nanyang Technological University (NTU) for the PhD scholarship. The authors would also like to thank the Nanyang Environment & Water Research Institute (NEWRI) staff for their assistance in instrument operations and analysis.

References

[1] W.X. Peng, L.S. Wang, M. Mirzaee, H. Ahmadi, M.J. Esfahani, S. Fremaux, Hydrogen and syngas production by catalytic biomass gasification, Energy Conversion and Management, 135 (2017) 270-273.
[2] B. Zhou, A. Dichiara, Y. Zhang, Q. Zhang, J. Zhou, Tar formation and evolution during biomass gasification: An experimental and theoretical study, Fuel, 234 (2018) 944-953.
[3] Y. Shen, K. Yoshikawa, Recent progresses in catalytic tar elimination during biomass gasification or pyrolysis—A review, Renewable and Sustainable Energy Reviews, 21 (2013) 371-392.
[4] K.-Y. Chiang, C.-H. Lu, M.-H. Lin, K.-L. Chien, Reducing tar yield in gasification of paper-reject sludge by using a hot-gas cleaning system, Energy, 50 (2013) 47-53.
[5] J. Han, H. Kim, The reduction and control technology of tar during biomass gasification/pyrolysis: An overview, Renewable and Sustainable Energy Reviews, 12 (2008) 397-416.

[6] L. Liu, Z. Zhang, S. Das, S. Kawi, Reforming of tar from biomass gasification in a hybrid catalysis-plasma system: A review, Applied Catalysis B: Environmental, 250 (2019) 250-272.
[7] B. Zhoufeng, D. Sonali, W.M. Hui, H. Plaifa, K. Sibudjing, A Review on Bimetallic Nickel-Based Catalysts for CO2 Reforming of Methane, ChemPhysChem, 18 (2017) 3117-3134.
[8] D.M. Argyle, H.C. Bartholomew, Heterogeneous Catalyst Deactivation and Regeneration: A Review, Catalysts, 5 (2015).
[9] X. Dou, A. Veksha, W.P. Chan, W.-D. Oh, Y.N. Liang, F. Teoh, D.K.B. Mohamed, A. Giannis, G. Lisak, T.-T. Lim, Poisoning effects of H2S and HCl on the naphthalene steam reforming and water-gas shift activities of Ni and Fe catalysts, Fuel, 241 (2019) 1008-1018.
[10] J.D. Ortego, J.T. Richardson, M.V. Twigg, Catalytic steam reforming of chlorocarbons: methyl chloride, Applied Catalysis B: Environmental, 12 (1997) 339-355.
[11] N. Couté, J.T. Richardson, Steam reforming of chlorocarbons: chlorinated aromatics, Applied Catalysis B: Environmental, 26 (2000) 217-226.
[12] A. Veksha, A. Giannis, W.-D. Oh, V.W.C. Chang, G. Lisak, T.-T. Lim, Catalytic activities and resistance to HCl poisoning of Ni-based catalysts during steam reforming of naphthalene, Applied Catalysis A: General, 557 (2018) 25-38.
[13] I.F. Elbaba, P.T. Williams, Deactivation of Nickel Catalysts by Sulfur and Carbon for the Pyrolysis–Catalytic Gasification/Reforming of Waste Tires for Hydrogen Production, Energy & Fuels, 28 (2014) 2104-2113.
[14] R. Chein, Z.-W. Yang, H2S effect on dry reforming of biogas for syngas production, International Journal of Energy Research, 43 (2019) 3330-3345.
[15] H. Madi, A. Lanzini, D. Papurello, S. Diethelm, C. Ludwig, M. Santarelli, J. Van herle, Solid oxide fuel cell anode degradation by the effect of hydrogen chloride in stack and single cell environments, Journal of Power Sources, 326 (2016) 349-356.
[16] U. Izquierdo, I. García-García, M.Á. Gutierrez, R.J. Arraibi, L.V. Barrio, F.J. Cambra, L.P. Arias, Catalyst Deactivation and Regeneration Processes in Biogas Tri-Reforming Process. The Effect of Hydrogen Sulfide Addition, Catalysts, 8 (2018).
[17] A.D. Hernandez, N. Kaisalo, P. Simell, M. Scarsella, Effect of H2S and thiophene on the steam reforming activity of nickel and rhodium catalysts in a simulated coke oven gas stream, Applied Catalysis B: Environmental, 258 (2019) 117977.
[18] D. Laprune, D. Farrusseng, Y. Schuurman, F.C. Meunier, J.A.Z. Pieterse, A.M. Steele, S. Thorpe, Effects of H2S and phenanthrene on the activity of Ni and Rh-based catalysts for the reforming of a simulated biomass-derived producer gas, Applied Catalysis B: Environmental, 221 (2018) 206-214.
[19] T.Y. Yeo, J. Ashok, S. Kawi, Recent developments in sulphur-resilient catalytic systems for syngas production, Renewable and Sustainable Energy Reviews, 100 (2019) 52-70.
[20] J.C. Rodriguez, E. Romeo, J.L.G. Fierro, J. Santamaría, A. Monzón, Deactivation by coking and poisoning of spinel-type Ni catalysts, Catal. Today, 37 (1997) 255-265.
[21] X. Chen, J. Jiang, F. Yan, K. Li, S. Tian, Y. Gao, H. Zhou, Dry Reforming of Model Biogas on a Ni/SiO2 Catalyst: Overall Performance and Mechanisms of Sulfur Poisoning and Regeneration, ACS Sustainable Chemistry & Engineering, 5 (2017) 10248-10257.
[22] M.D. Krcha, K.M. Dooley, M.J. Janik, Alkane reforming on partially sulfided CeO2 (111) surfaces, Journal of Catalysis, 330 (2015) 167-176.
[23] C. Gillan, M. Fowles, S. French, S.D. Jackson, Ethane Steam Reforming over a Platinum/Alumina Catalyst: Effect of Sulfur Poisoning, Industrial & Engineering Chemistry Research, 52 (2013) 13350-13356.
[24] S. Cimino, L. Lisi, G. Mancino, Effect of phosphorous addition to Rh-supported catalysts for the dry reforming of methane, International Journal of Hydrogen Energy, 42 (2017) 23587-23598.
[25] F.L. Chan, A. Tanksale, Review of recent developments in Ni-based catalysts for biomass gasification, Renewable and Sustainable Energy Reviews, 38 (2014) 428-438.

[26] C.P.B. Quitete, R.L. Manfro, M.M.V.M. Souza, Perovskite-based catalysts for tar removal by steam reforming: Effect of the presence of hydrogen sulfide, International Journal of Hydrogen Energy, 42 (2017) 9873-9880.

[27] U. Izquierdo, I. García-García, Á.M. Gutierrez, J.R. Arraibi, V.L. Barrio, J.F. Cambra, P.L. Arias, Catalyst Deactivation and Regeneration Processes in Biogas Tri-Reforming Process. The Effect of Hydrogen Sulfide Addition, Catalysts, 8 (2018) 12.

[28] S.L. Lakhapatri, M.A. Abraham, Analysis of catalyst deactivation during steam reforming of jet fuel on Ni-(PdRh)/γ-Al2O3 catalyst, Applied Catalysis A: General, 405 (2011) 149-159.

[29] K. Sato, K. Fujimoto, Development of new nickel based catalyst for tar reforming with superior resistance to sulfur poisoning and coking in biomass gasification, Catalysis Communications, 8 (2007) 1697-1701.

[30] C.A. Schwengber, F.A. da Silva, R.A. Schaffner, N.R.C. Fernandes-Machado, R.J. Ferracin, V.R. Bach, H.J. Alves, Methane dry reforming using Ni/Al2O3 catalysts: Evaluation of the effects of temperature, space velocity and reaction time, Journal of Environmental Chemical Engineering, 4 (2016) 3688-3695.

[31] Z. Zhang, L. Liu, B. Shen, C. Wu, Preparation, modification and development of Ni-based catalysts for catalytic reforming of tar produced from biomass gasification, Renewable and Sustainable Energy Reviews, 94 (2018) 1086-1109.

[32] S.H. Feng, G.H. Li, Chapter 4 - Hydrothermal and Solvothermal Syntheses, in: R. Xu, Y. Xu (Eds.) Modern Inorganic Synthetic Chemistry (Second Edition), Elsevier, Amsterdam, 2017, pp. 73-104.

[33] M. Adachi-Pagano, C. Forano, J.-P. Besse, Synthesis of Al-rich hydrotalcite-like compounds by using the urea hydrolysis reaction—control of size and morphology, Journal of Materials Chemistry, 13 (2003) 1988-1993.

[34] L.H. Chagas, G.S.G. De Carvalho, W.R. Do Carmo, R.A.S. San Gil, S.S.X. Chiaro, A.A. Leitão, R. Diniz, L.A. De Sena, C.A. Achete, MgCoAl and NiCoAl LDHs synthesized by the hydrothermal urea hydrolysis method: Structural characterization and thermal decomposition, Materials Research Bulletin, 64 (2015) 207-215.

[35] W. Wang, X. Huang, S. Wu, Y. Zhou, L. Wang, H. Shi, Y. Liang, B. Zou, Preparation of p–n junction Cu2O/BiVO4 heterogeneous nanostructures with enhanced visible-light photocatalytic activity, Applied Catalysis B: Environmental, 134-135 (2013) 293-301.

[36] S. Li, H. Zhu, Z. Qin, G. Wang, Y. Zhang, Z. Wu, Z. Li, G. Chen, W. Dong, Z. Wu, L. Zheng, J. Zhang, T. Hu, J. Wang, Morphologic effects of nano CeO2–TiO2 on the performance of Au/CeO2–TiO2 catalysts in low-temperature CO oxidation, Applied Catalysis B: Environmental, 144 (2014) 498-506.

[37] Z. Yang, Y. Huang, D. Ji, G. Xiong, H. Luo, Y. Wan, Hydrazine hydrate-induced hydrothermal synthesis of MnFe2O4 nanoparticles dispersed on graphene as high-performance anode material for lithium ion batteries, Ceramics International, 43 (2017) 10905-10912.

[38] J. Yang, S. Mei, J.M.F. Ferreira, Hydrothermal Synthesis of Nanosized Titania Powders: Influence of Tetraalkyl Ammonium Hydroxides on Particle Characteristics, Journal of the American Ceramic Society, 84 (2001) 1696-1702.

[39] Q. Zhang, T. Wu, P. Zhang, R. Qi, R. Huang, X. Song, L. Gao, Facile synthesis of hollow hierarchical Ni/γ-Al2O3 nanocomposites for methane dry reforming catalysis, RSC Advances, 4 (2014) 51184-51193.

[40] Z. Bian, S. Kawi, Highly carbon-resistant Ni–Co/SiO2 catalysts derived from phyllosilicates for dry reforming of methane, Journal of CO2 Utilization, 18 (2017) 345-352.

[41] R. Coll, J. Salvadó, X. Farriol, D. Montané, Steam reforming model compounds of biomass gasification tars: conversion at different operating conditions and tendency towards coke formation, Fuel Processing Technology, 74 (2001) 19-31.

[42] B. Abdullah, N.A. Abd Ghani, D.-V.N. Vo, Recent advances in dry reforming of methane over Ni-based catalysts, Journal of Cleaner Production, 162 (2017) 170-185.

[43] W.P. Chan, A. Veksha, J. Lei, W.-D. Oh, X. Dou, A. Giannis, G. Lisak, T.-T. Lim, A hot syngas purification system integrated with downdraft gasification of municipal solid waste, Applied Energy, 237 (2019) 227-240.
[44] R.-S. Zhou, R.L. Snyder, Structures and transformation mechanisms of the [eta], [gamma] and [theta] transition aluminas, Acta Crystallographica Section B, 47 (1991) 617-630.
[45] X. Li, G.M. Kale, Urea-based hydrothermal synthesis of ITO nanopowders, Journal of Physics: Conference Series, 26 (2006) 319-322.
[46] X.Y. Chen, Z.J. Zhang, X.L. Li, S.W. Lee, Controlled hydrothermal synthesis of colloidal boehmite (γ-AlOOH) nanorods and nanoflakes and their conversion into γ- Al2O3 nanocrystals, Solid State Communications, 145 (2008) 368-373.
[47] X. Hu, P. Li, X. Zhang, B. Yu, C. Lv, N. Zeng, J. Luo, Z. Zhang, J. Song, Y. Liu, Ni-Based Catalyst Derived from NiAl Layered Double Hydroxide for Vapor Phase Catalytic Exchange between Hydrogen and Water, Nanomaterials, 9 (2019).
[48] Z. Shang, S. Li, L. Li, G. Liu, X. Liang, Highly active and stable alumina supported nickel nanoparticle catalysts for dry reforming of methane, Applied Catalysis B: Environmental, 201 (2017) 302-309.
[49] L. Samain, A. Jaworski, M. Edén, D.M. Ladd, D.-K. Seo, F. Javier Garcia-Garcia, U. Häussermann, Structural analysis of highly porous γ-Al2O3, Journal of Solid State Chemistry, 217 (2014) 1-8.
[50] S.V. Moghaddam, M. Rezaei, F. Meshkani, Surfactant-Free Sol–Gel Synthesis Method for the Preparation of Mesoporous High Surface Area NiO–Al2O3 Nanopowder and Its Application in Catalytic CO2 Methanation, Energy Technology, 8 (2020) 1900778.
[51] A. Lechkar, A. Barroso Bogeat, G. Blanco, J.M. Pintado, M. Soussi el Begrani, Methanation of carbon dioxide over ceria-praseodymia promoted Ni-alumina catalysts. Influence of metal loading, promoter composition and alumina modifier, Fuel, 234 (2018) 1401-1413.
[52] R.-j. Zhang, G.-f. Xia, M.-f. Li, Y. Wu, H. Nie, D.-d. Li, Effect of support on the performance of Ni-based catalyst in methane dry reforming, Journal of Fuel Chemistry and Technology, 43 (2015) 1359-1365.
[53] C. Jiménez-González, Z. Boukha, B. de Rivas, J.R. González-Velasco, J.I. Gutiérrez-Ortiz, R. López-Fonseca, Behavior of Coprecipitated NiAl2O4/Al2O3 Catalysts for Low-Temperature Methane Steam Reforming, Energy & Fuels, 28 (2014) 7109-7121.
[54] A. Remiro, A. Arandia, L. Oar-Arteta, J. Bilbao, A.G. Gayubo, Regeneration of NiAl2O4 spinel type catalysts used in the reforming of raw bio-oil, Applied Catalysis B: Environmental, 237 (2018) 353-365.
[55] A.P. Grosvenor, M.C. Biesinger, R.S.C. Smart, N.S. McIntyre, New interpretations of XPS spectra of nickel metal and oxides, Surface Science, 600 (2006) 1771-1779.
[56] L. Zhang, X. Wang, C. Chen, X. Zou, W. Ding, X. Lu, Dry reforming of methane to syngas over lanthanum-modified mesoporous nickel aluminate/γ-alumina nanocomposites by one-pot synthesis, International Journal of Hydrogen Energy, 42 (2017) 11333-11345.
[57] F. Qin, J.W. Anderegg, C.J. Jenks, B. Gleeson, D.J. Sordelet, P.A. Thiel, X-ray photoelectron spectroscopy studies of the early-stage oxidation behavior of (Pt, Ni)3Al(111) surfaces in air, Surface Science, 602 (2008) 205-215.
[58] J.F. Moulder, Handbook of X-Ray Photoelectron Spectroscopy, Physical Electronics, (1995) 230-232.
[59] M.H. Amin, S. Putla, S. Bee Abd Hamid, S.K. Bhargava, Understanding the role of lanthanide promoters on the structure–activity of nanosized Ni/γ-Al2O3 catalysts in carbon dioxide reforming of methane, Applied Catalysis A: General, 492 (2015) 160-168.
[60] C.-F. Sun, B.J. Glaz, M. Okada, E. Baker III, X.-Y. Cheng, S.P. Karna, Y. Wang, Blocking Oxidation Failures of Carbon Nanotubes through Selective Protection of Defects, Advanced Materials, 28 (2016) 6672-6679.

[61] K.A. Wepasnick, B.A. Smith, J.L. Bitter, D. Howard Fairbrother, Chemical and structural characterization of carbon nanotube surfaces, Analytical and Bioanalytical Chemistry, 396 (2010) 1003-1014.

[62] M.H. Amin, Relationship Between the Pore Structure of Mesoporous Silica Supports and the Activity of Nickel Nanocatalysts in the CO2 Reforming of Methane, Catalysts, 10 (2020) 51.

[63] A. Ochoa, J. Bilbao, A.G. Gayubo, P. Castaño, Coke formation and deactivation during catalytic reforming of biomass and waste pyrolysis products: A review, Renewable and Sustainable Energy Reviews, 119 (2020) 109600.

[64] J. Vicente, C. Montero, J. Ereña, M.J. Azkoiti, J. Bilbao, A.G. Gayubo, Coke deactivation of Ni and Co catalysts in ethanol steam reforming at mild temperatures in a fluidized bed reactor, International Journal of Hydrogen Energy, 39 (2014) 12586-12596.

[65] C. Montero, A. Remiro, B. Valle, L. Oar-Arteta, J. Bilbao, A.G. Gayubo, Origin and Nature of Coke in Ethanol Steam Reforming and Its Role in Deactivation of Ni/La2O3–αAl2O3 Catalyst, Industrial & Engineering Chemistry Research, 58 (2019) 14736-14751.

[66] M. Riegraf, M.P. Hoerlein, R. Costa, G. Schiller, K.A. Friedrich, Sulfur Poisoning of Electrochemical Reformate Conversion on Nickel/Gadolinium-Doped Ceria Electrodes, ACS Catalysis, 7 (2017) 7760-7771.

[67] G. Garbarino, A. Romero Perez, E. Finocchio, G. Busca, A study of the deactivation of low loading Ni/Al2O3 steam reforming catalyst by tetrahydrothiophene, Catalysis Communications, 38 (2013) 67-73.

[68] J. Blanchard, I. Achouri, N. Abatzoglou, H2S poisoning of NiAl2O4/Al2O3-YSZ catalyst during methane dry reforming, The Canadian Journal of Chemical Engineering, 94 (2016) 650-654.

[69] S. Appari, V.M. Janardhanan, R. Bauri, S. Jayanti, Deactivation and regeneration of Ni catalyst during steam reforming of model biogas: An experimental investigation, International Journal of Hydrogen Energy, 39 (2014) 297-304.

[70] X. Yang, An experimental investigation on the deactivation and regeneration of a steam reforming catalyst, Renewable Energy, 112 (2017) 17-24.

[71] T.W. Hansen, A.T. DeLaRiva, S.R. Challa, A.K. Datye, Sintering of Catalytic Nanoparticles: Particle Migration or Ostwald Ripening?, Accounts of Chemical Research, 46 (2013) 1720-1730.

[72] A.T. DeLaRiva, T.W. Hansen, S.R. Challa, A.K. Datye, In situ Transmission Electron Microscopy of catalyst sintering, Journal of Catalysis, 308 (2013) 291-305.

[73] J. Du, J. Gao, F. Gu, J. Zhuang, B. Lu, L. Jia, G. Xu, Q. Liu, F. Su, A strategy to regenerate coked and sintered Ni/Al2O3 catalyst for methanation reaction, International Journal of Hydrogen Energy, 43 (2018) 20661-20670.

[74] Y. Liu, J. Gao, Q. Liu, F. Gu, X. Lu, L. Jia, G. Xu, Z. Zhong, F. Su, Preparation of high-surface-area Ni/α-Al2O3 catalysts for improved CO methanation, RSC Advances, 5 (2015) 7539-7546.

[75] D. Li, M. Koike, L. Wang, Y. Nakagawa, Y. Xu, K. Tomishige, Regenerability of Hydrotalcite-Derived Nickel–Iron Alloy Nanoparticles for Syngas Production from Biomass Tar, ChemSusChem, 7 (2014) 510-522.

[76] L. Foppa, T. Margossian, S.M. Kim, C. Müller, C. Copéret, K. Larmier, A. Comas-Vives, Contrasting the Role of Ni/Al2O3 Interfaces in Water–Gas Shift and Dry Reforming of Methane, J. Am. Chem. Soc., 139 (2017) 17128-17139.

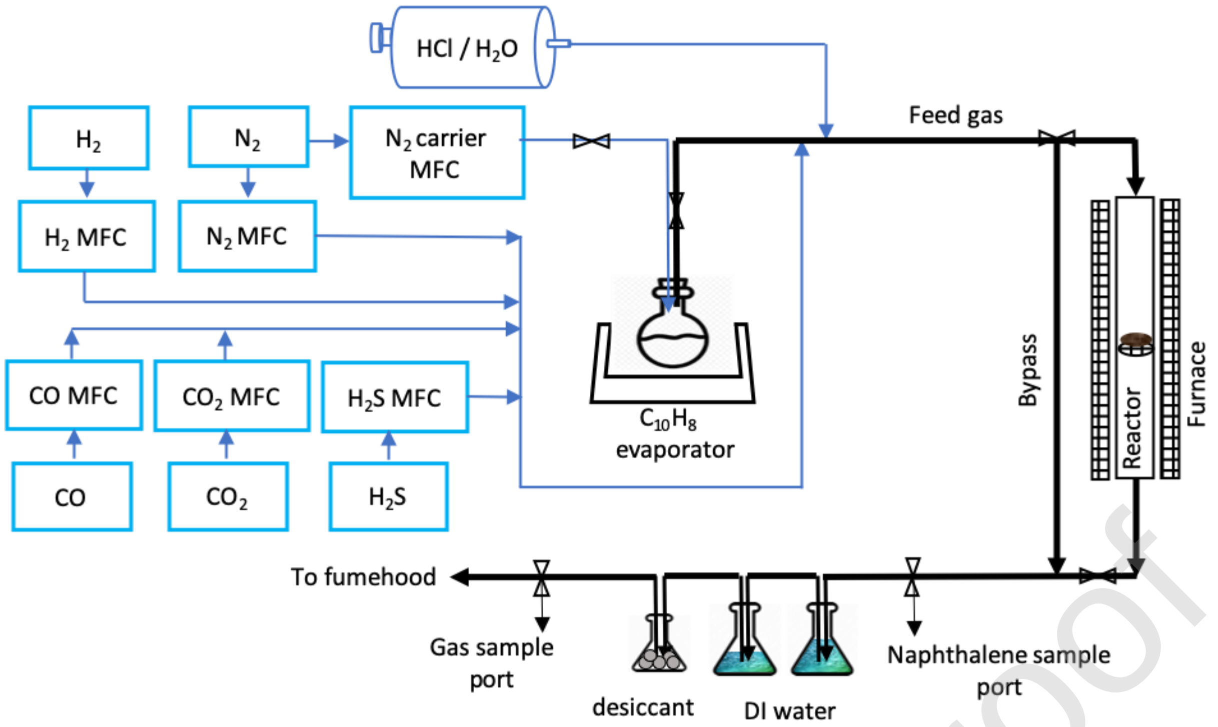

Fig. 1. Bench-scale catalytic steam reforming setup.

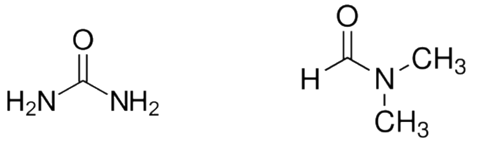

urea N,N'-dimethylformamide

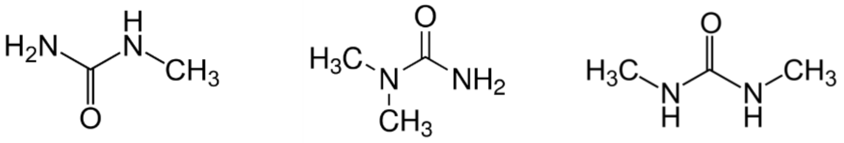

N-methylurea 1,1-dimethylurea N,N'-dimethylurea

Fig. 2. Chemical structures of precipitants used for catalysts synthesis.

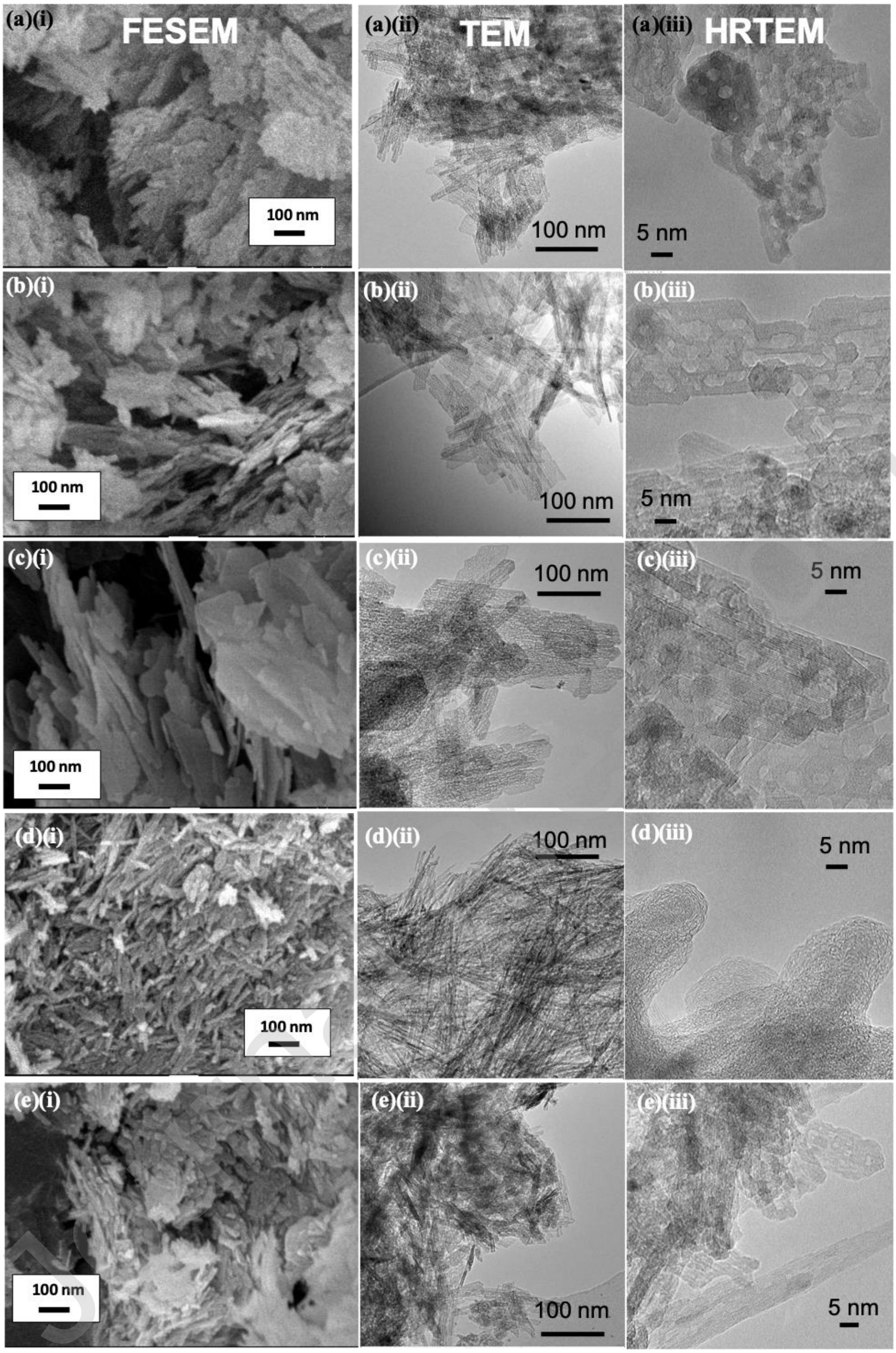

Fig. 3. FESEM, TEM and HRTEM images of (a) Ni(*ur*), (b) Ni(*mur*), (c) Ni(*mmur*), (d) Ni(*dmf*) and Ni(*dmur*) catalysts.

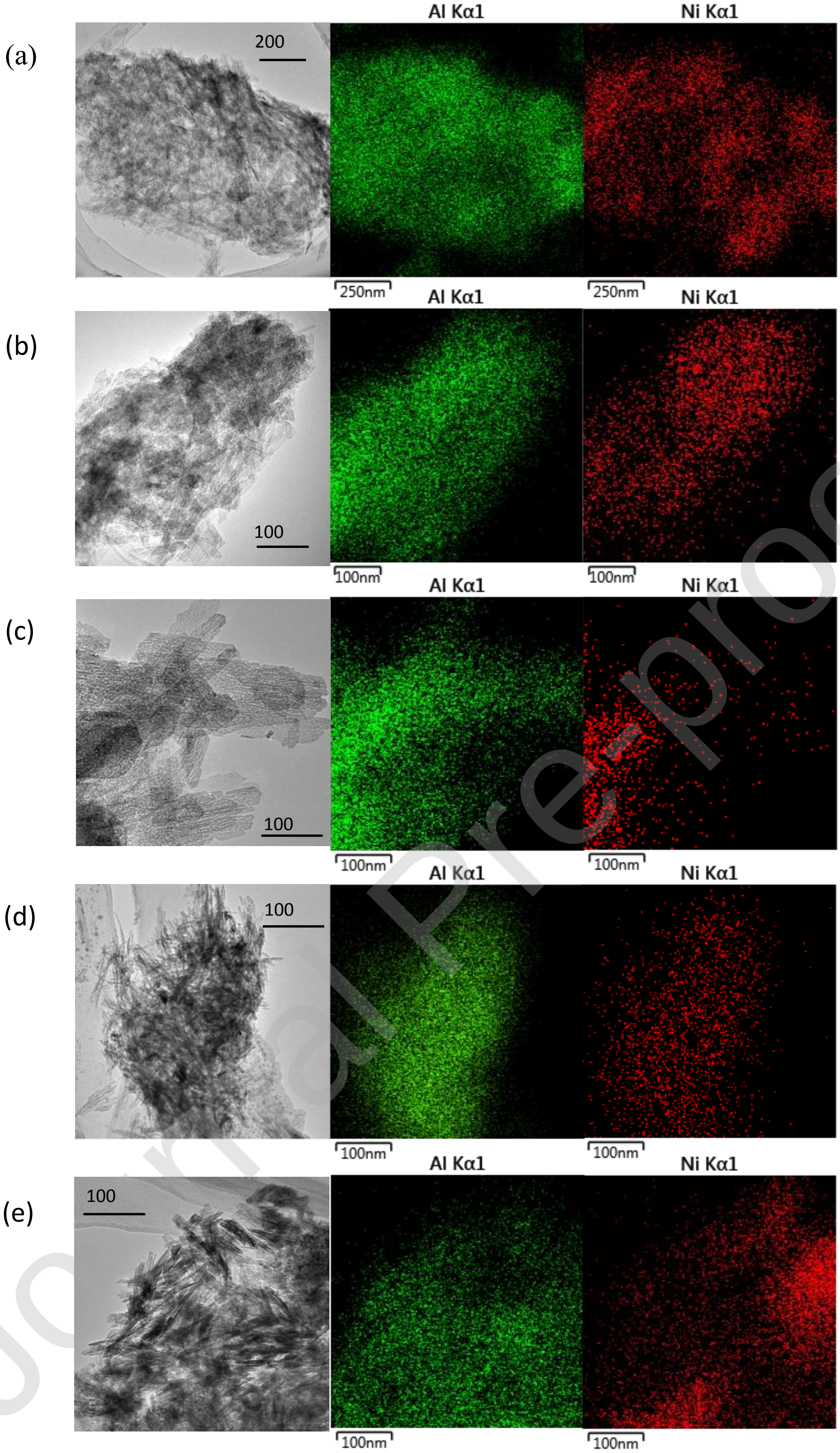

Fig. 4. TEM-EDS images of (a) Ni(*ur*), (b) Ni(*mur*), (c) Ni(*mmur*), (d) Ni(*dmf*) and (e) Ni(*dmur*) showing the dispersion of Ni over the alumina support.

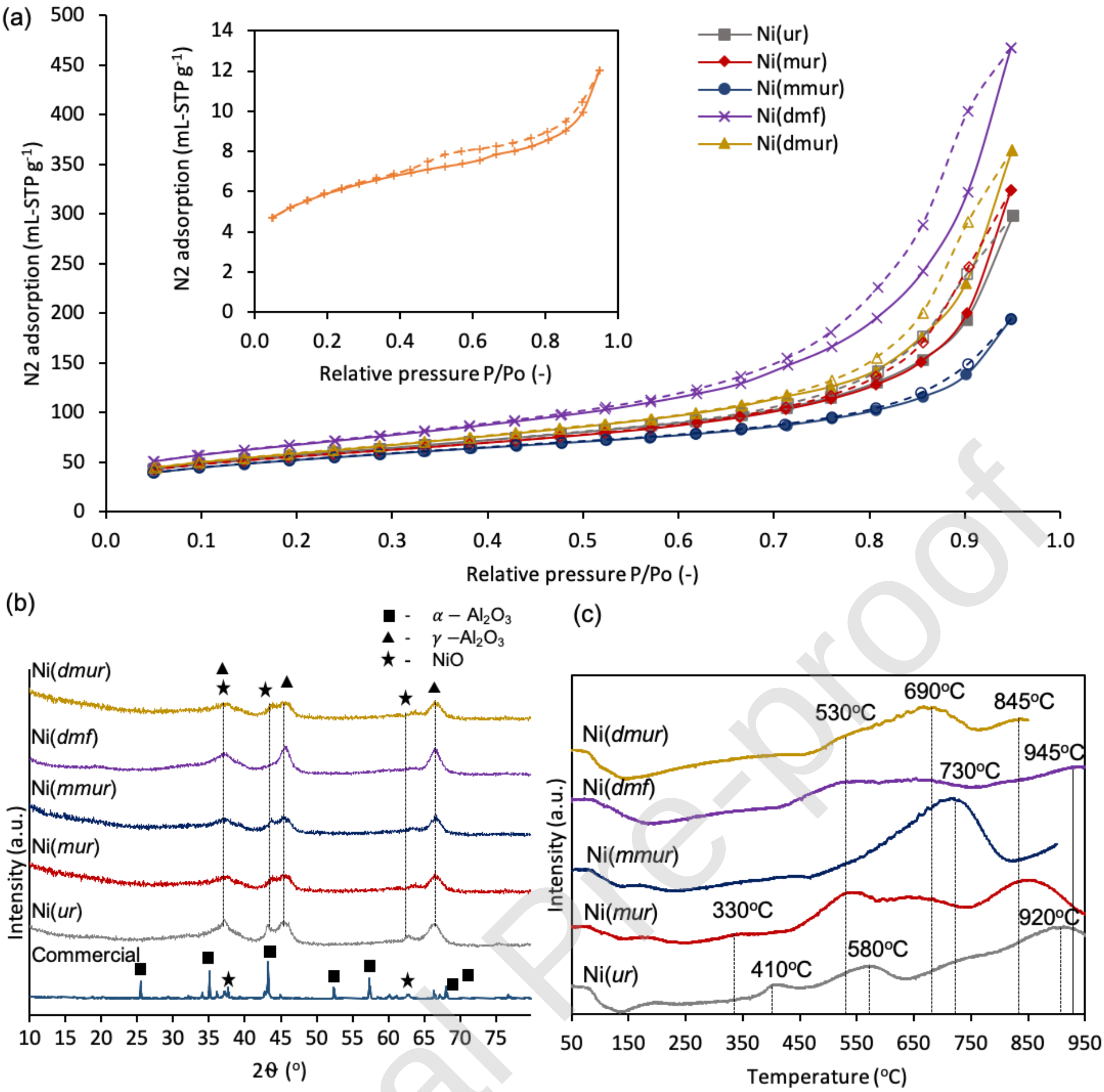

Fig. 5. (a) N_2 isotherms of synthesized catalysts. Inset: N_2 isotherm of commercial catalyst. (b) XRD spectra of the commercial and synthesized catalysts. (c) TPR profiles of developed catalysts.

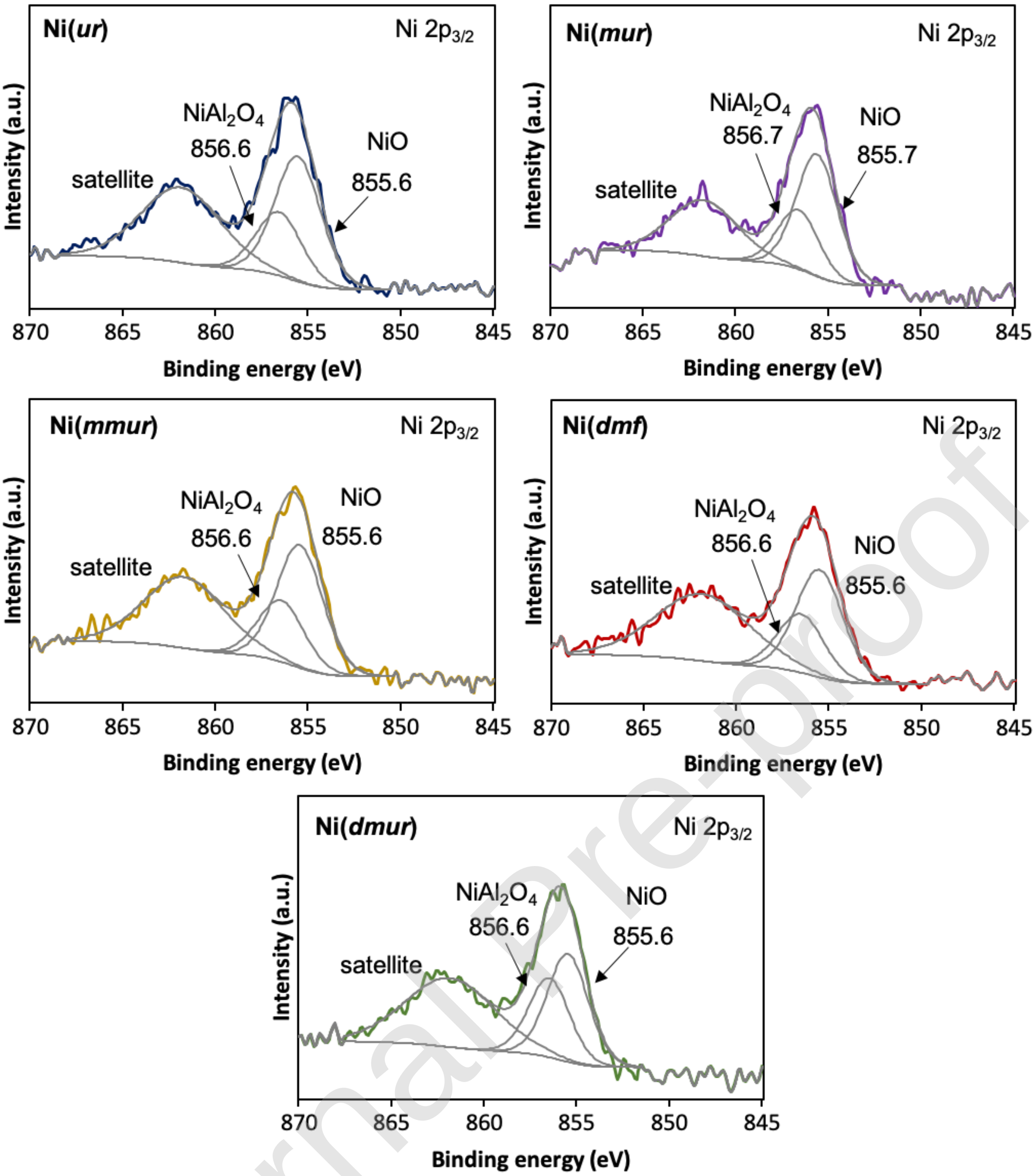

Fig. 6. Ni 2p XPS profiles of the commercial and synthesized catalysts.

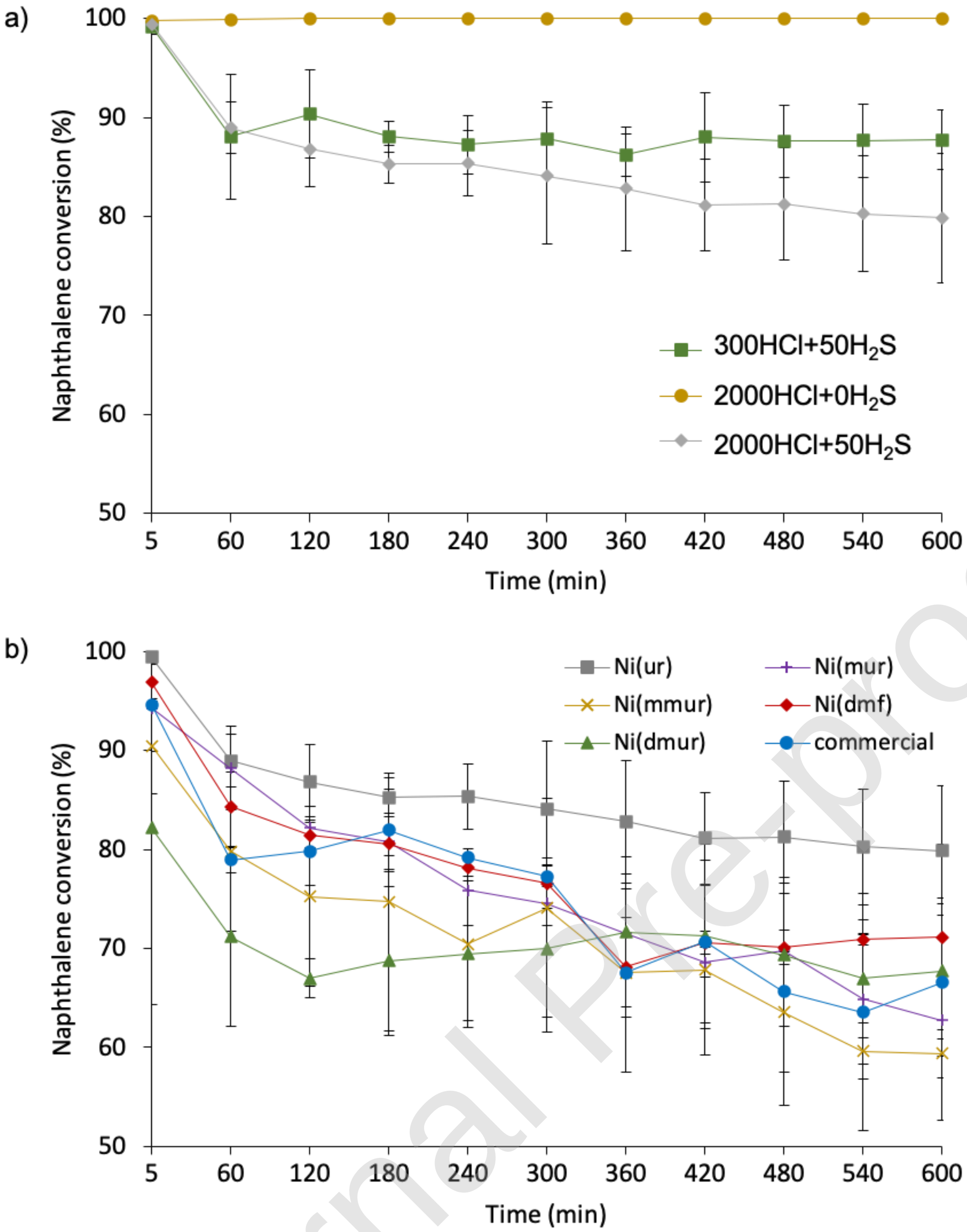

Fig. 7. Naphthalene conversion a) over Ni(ur) at different conditions and b) over various catalyst at 2000 ppmv HCl and 50 ppmv H_2S at 800 °C.

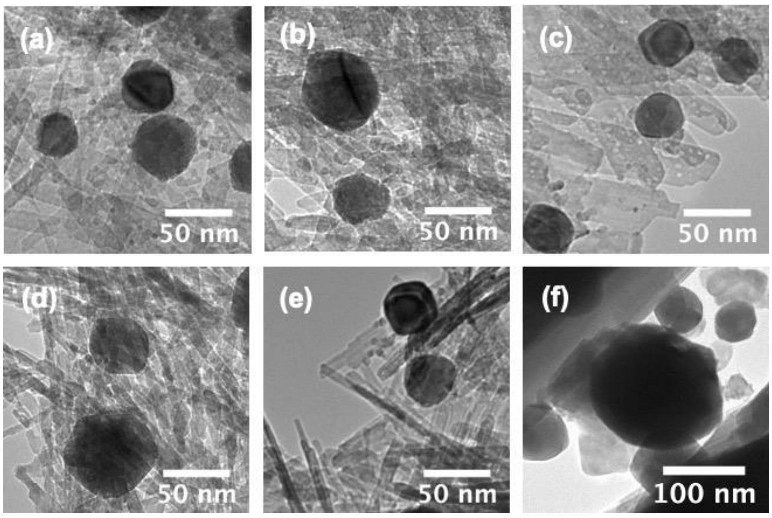

Fig. 8. TEM of Ni particles in the spent catalysts after 10 h reforming: (a) Ni(*ur*), (b) Ni(*dmf*), (c) Ni(*dmur*), (d) Ni(*mur*), (e) Ni(*mmur*), and (f) commercial (Experimental conditions: 0.055 vol. % naphthalene, 24 vol. % H_2O, 9 vol. % H_2, 10 vol%. CO, 9 vol. % CO_2, 50 ppmv H_2S, 2000 ppmv HCl at 800 °C).

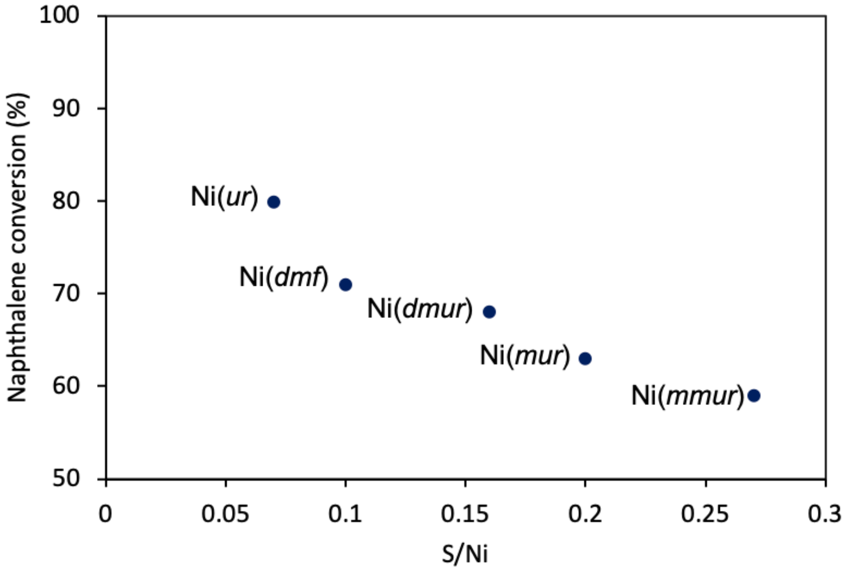

Fig. 9. Reforming activity of catalysts based on Ni coverage by S (Experimental conditions: 0.055 vol. % naphthalene, 24 vol. % H_2O, 9 vol. % H_2, 10 vol%. CO, 9 vol. % CO_2, 50 ppmv H_2S, 2000 ppmv HCl at 800 °C).

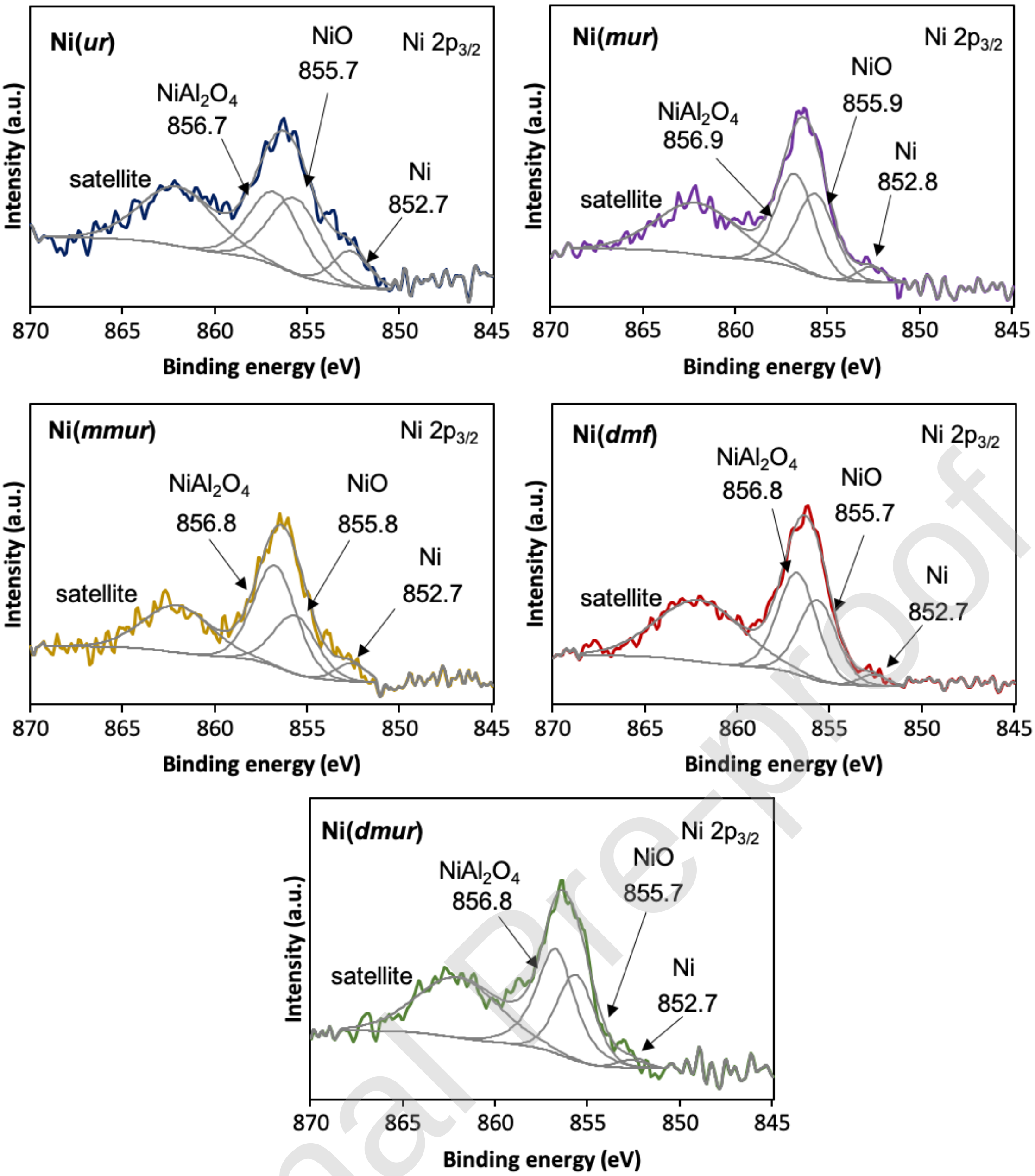

Fig. 10. Ni 2p XPS profiles of the spent catalysts (Experimental conditions: 0.055 vol. % naphthalene, 24 vol. % H_2O, 9 vol. % H_2, 10 vol%. CO, 9 vol. % CO_2, 50 ppmv H_2S, 2000 ppmv HCl at 800 °C).

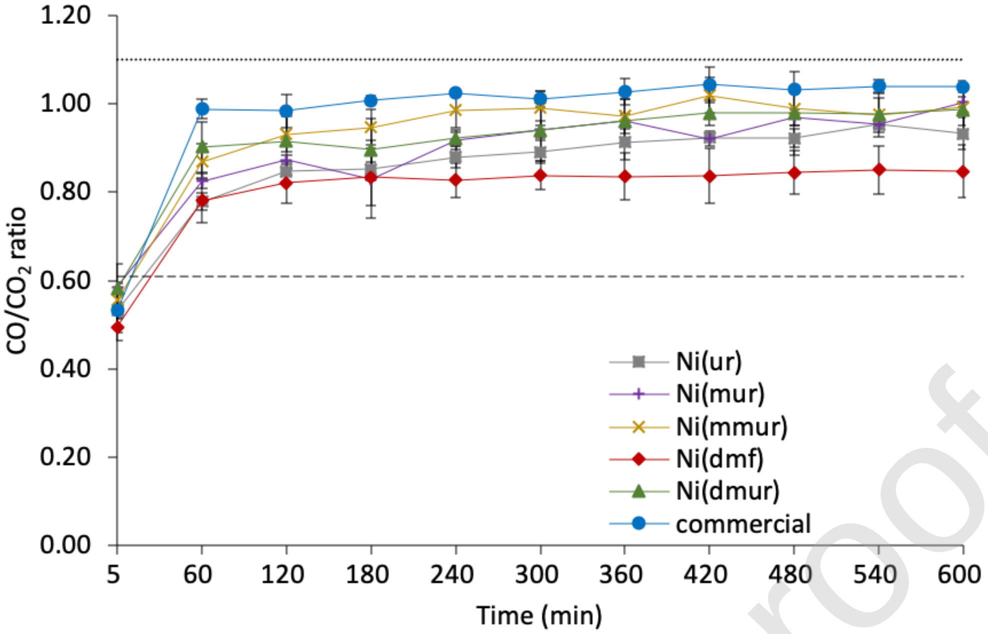

Fig. 11. CO/CO_2 ratios in product gas over various catalyst. Dashed lines: CO/CO_2 =0.61 at thermodynamic equilibrium. Dotted lines: CO/CO_2 =1.10 at gas feed (Experimental conditions: 0.055 vol. % naphthalene, 24 vol. % H_2O, 9 vol. % H_2, 10 vol%. CO, 9 vol. % CO_2, 0 or 50 ppmv H_2S, 2000 ppmv HCl at 800 °C).

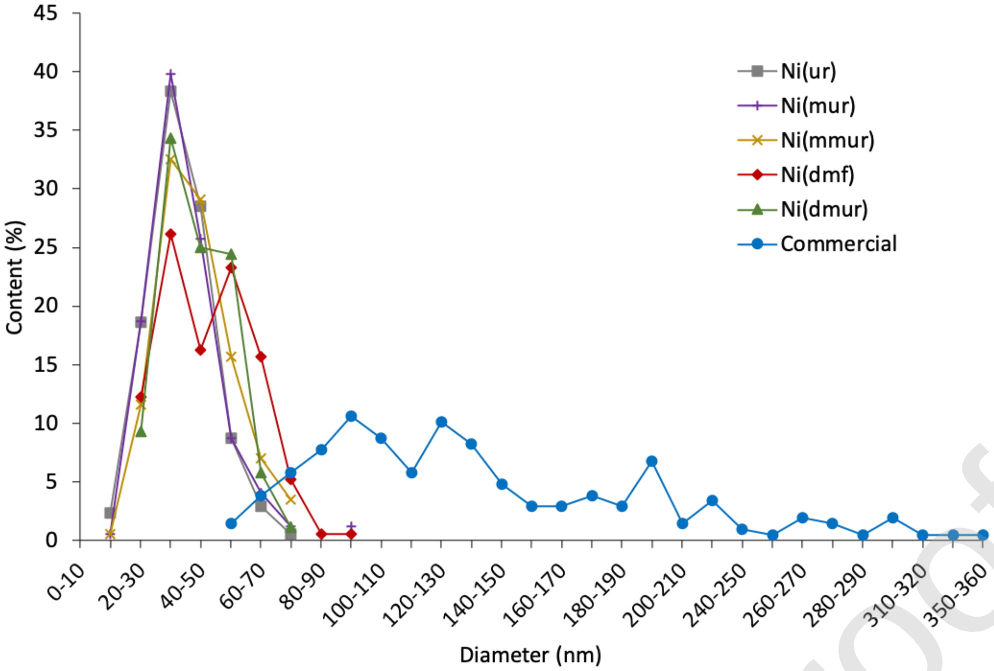

Fig. 12. Size distribution of nickel nanoparticles in comparison with commercial catalyst after 10 h (Experimental conditions: 0.055 vol. % naphthalene, 24 vol. % H_2O, 9 vol. % H_2, 10 vol%. CO, 9 vol. % CO_2, 50 ppmv H_2S, 2000 ppmv HCl at 800 °C).

Table 1. Properties of fresh catalysts.

Catalyst	**Ni/Al molar ratio**	**Ni (wt.%)[a]**	**Bulk density (g mL^{-1})**	**Ni load per bed volume (g 0.5 mL^{-1})**	**BET surface area (m^2 g^{-1})**	**Total pore volume (mL g^{-1})[b]**
Ni(*ur*)	0.12	9.8	0.62	0.030	200	0.413
Ni(*mur*)	0.12	9.7	0.51	0.025	195	0.459
Ni(*mmur*)	0.12	10.2	0.48	0.025	183	0.242
Ni(*dmf*)	0.12	8.7	0.52	0.023	243	0.696
Ni(*dmur*)	0.12	9.8	0.56	0.028	210	0.523
Commercial	-	15.9	1.55	0.123	20	0.01

[a] From ICP-OES analysis. [b] Based on nitrogen adsorption isotherms.

Table 2. Distribution of surface Ni^{2+} and corresponding binding energies in the fresh catalysts.

Catalyst	**Peak 1**		**Peak 2**	
	Content (%)	**Binding energy (eV)**	**Content (%)**	**Binding energy (eV)**
Ni(*ur*)	66.3	855.6	33.7	856.6
Ni(*mur*)	67.4	855.7	32.6	856.7
Ni(*mmur*)	66.6	855.6	33.4	856.6
Ni(*dmf*)	64.8	855.6	35.2	856.6
Ni(*dmur*)	57.7	855.6	42.3	856.6

Table 3. Distribution of surface Ni^0 and Ni^{2+} and corresponding binding energies in the spent catalysts.

Catalyst	**Peak 1**		**Peak 2**		**Peak 3**		**Peak 1+3**
	Content (%)	**Binding energy (eV)**	**Content (%)**	**Binding energy (eV)**	**Content (%)**	**Binding energy (eV)**	**Content (%)**
Ni(*ur*)	15.3	852.7	34.5	855.7	50.2	856.7	65.5
Ni(*mur*)	7.3	852.8	42.1	855.9	50.5	856.9	57.8
Ni(*mmur*)	8.4	852.7	43.1	855.8	48.5	856.8	56.9
Ni(*dmf*)	3.8	852.7	36.7	855.7	59.5	856.8	63.3
Ni(*dmur*)	1.7	852.7	40.9	855.7	57.5	856.8	59.2

Table 4. Comparison of reforming activity of selected reported catalysts.

Catalyst	**Conditions**	**Impurity**	**Conversion (%)**	**Ref.**
Ni(*ur*)	T: 800 °C, Time: 10 h Gas composition: Naphthalene – 0.055 vol.%, H_2O – 24 vol.%, H_2 – 9 vol.%, CO – 10 vol.%, CO_2 – 9 vol.% GHSV: 24000 h^{-1}	2000 ppmv HCl, 50 ppmv H_2S	80	This work
Commercial (Ni/Al_2O_3)	T: 800 °C, Time: 10 h Gas composition: Naphthalene – 0.055 vol.%, H_2O – 24 vol.%, H_2 – 9 vol.%, CO – 10 vol.%, CO_2 – 9 vol.% GHSV: 24000 h^{-1}	2000 ppmv HCl, 50 ppmv H_2S	67	This work
0Fe0.4Ni/Al	T: 790 °C, Time: 5 h Gas composition: Naphthalene – 0.14 vol.%, H_2 – 10 vol.%, H_2O – 26 vol.% GHSV: 24000 h^{-1}	300 ppmv HCl, 50 ppmv H_2S	~40	[9]
Ni/Al_2O_3	T: 800 °C, Time: 2 h Gas composition: Benzene – 0.1 vol.%, H_2 – 50 vol.%, H_2O – 48.7 vol.%, CO – 5.3 vol.% GHSV: 76000 h^{-1}	50 ppmv H_2S	14	[17]
$Ni/\gamma\text{-}Al_2O_3$	T: 800 °C, Time: 11 h Gas composition: $H_2O/CH_4 = 2.02$, $CH_4/CO_2 = 1.49$	50 ppmv H_2S	43	[69]
$Ni\text{-}Ce/\alpha\text{-}Al_2O_3$	T: 800 °C, Time: 20 h Gas composition: $H_2O/CH_4 = 3$	30 ppm H_2S	~55	[70]
$Rh\text{-}Ni/Ce\text{-}Al_2O_3$	T: 800 °C, Time: 3 h Gas composition: $H_2O/CH_4+CO_2 = 1$, $O/\ CH_4+CO_2 = 0.25$ WHSV: 161 $g_{gas}\cdot g_{cat}\ h^{-1}$	25 ppmv H_2S	~30	[27]
$LaNi_{0.5}Mn_{0.5}O_3$	T: 800 °C, Time: 10 h Gas composition: H_2O/toluene = 3 GHSV: 20000 $mLg^{-1}h^{-1}$	50 ppm H_2S	~42	[26]